Effects of substrate composition and subsurface fluid pathways on the geochemistry of seafloor hydrothermal deposits at the Lucky Strike Vent Field, Mid-Atlantic Ridge

Dennis Sánchez-mora, John Jamieson, Mathilde Cannat, Javier Escartin, Thibaut Barreyre

Effects of substrate composition and subsurface fluid pathways on the geochemistry of seafloor hydrothermal deposits at the Lucky Strike Vent Field, Mid-Atlantic Ridge

Dennis Sánchez-Mora[1], John Jamieson[1], Mathilde Cannat[2], Javier Escartín[3], and Thibaut Barreyre[4]

[1] Department of Earth Sciences, Memorial University of Newfoundland, St. John's, Newfoundland and Labrador, A1B 3X7, Canada.

[2] Université de Paris, Institut de Physique du Globe de Paris, UMR 7154 CNRS, France.

[3] Laboratoire de Géologie – CNRS, UMR 8538, École Normale Supérieure, PSL University, Paris, France.

[4] Department of Earth Science/K.G. Jebsen Centre for Deep Sea Research, University of Bergen, Bergen, Norway.

Corresponding author: Dennis Sánchez-Mora (dsanchezmora@mun.ca)

Key Points:

- Spatial variations in *in situ* sulfur isotope compositions at Lucky Strike indicate differences in fluid/rock interactions in the sub-surface.
- *In situ* sulfur isotope data suggests that >80% of the available H_2S in the ascending hydrothermal fluid has precipitated in the subseafloor.
- The Ba/Co ratio of hydrothermal deposits discriminates those associated with E-MORBs from other mafic/ultramafic hosted deposits.

This article has been accepted for publication and undergone full peer review but has not been through the copyediting, typesetting, pagination and proofreading process, which may lead to differences between this version and the Version of Record. Please cite this article as doi: 10.1029/2021GC010073.

Abstract

The Lucky Strike vent field, located on the Mid-Atlantic Ridge (MAR), is hosted on enriched mid-ocean ridge basalt associated with the nearby Azores hotspot. In this study, we present bulk rock geochemistry coupled with *in situ* sulfur isotope analysis of hydrothermal samples from Lucky Strike. We assess the geological controls on the differences in the major and trace element content and sulfur isotopic composition of the hydrothermal deposits within the vent field. The hydrothermal deposits contain elevated concentrations of elements typically enriched in E-MORB, such as Mo, Ba, and Sr, compared to typical values for other hydrothermal deposits hosted on the MAR. The range in sulfur isotope compositions of hydrothermal marcasite and chalcopyrite (-2.5 to 8.7‰) is similar to the range recorded at other sediment-free basalt-hosted seafloor hydrothermal sites. However, at Lucky Strike, the Capelinhos vent, situated 1.4 km east of the main field, is enriched in ^{34}S (by ~3.5‰ for both marcasite and chalcopyrite), relative to the main field. This difference reflects contrasting subseafloor fluid/rock interactions at these two sites, including subseafloor sulfide precipitation at the main field that results in <20% of reduced sulfur within the upwelling hydrothermal fluid reaching the seafloor. We also compare the geochemistry of the hydrothermal deposits at Lucky Strike to other hydrothermal sites along the MAR and show that the average hydrothermal deposit Ba/Co is useful to discriminate between E-MORB and other mafic/ultramafic hosted deposits.

Plain Language Summary

We investigate the variations in composition of metal- and sulfur-rich hydrothermal deposits that form on the seafloor at a cluster of high-temperature hot springs called the Lucky Strike hydrothermal vent field, on the Mid-Atlantic Ridge. We find that the mineralogy and geochemistry of the deposits do not vary spatially within this vent field. However, variations in the relative abundances of different sulfur isotopes within these deposits differ between the central cluster of vents and a newly discovered site called Capelinhos that is located 1.4 km east of the main vent field. Isotopic variations are usually interpreted to indicate differences in sulfur sources, with seawater and sulfur from the mantle as the two primary sources. However, our results instead show that significant mineral precipitation below the seafloor at the main vent cluster is the likely source of these isotopic variations.

In addition, we show that the relative abundances of various trace elements within the hydrothermal deposits can be used to fingerprint the composition of the volcanic rocks that host these deposits. In particular, the ratio of Ba to Co can be used to fingerprint specific tectonic settings for different hydrothermal vent sites on mid-ocean ridges.

1. Introduction

Subseafloor magmatism drives hydrothermal circulation and the formation of metal and sulfur-rich mineral deposits at or below the seafloor (Hannington, 2014; Lydon, 1988; Tivey, 2007). The geochemistry of seafloor hydrothermal deposits is controlled by several factors, including the

composition of the subseafloor lithosphere with which the circulating fluids react, temperature, pressure, the presence and type of sediment, and magmatic volatile input into the system (Doe, 1994; Hannington et al., 1995, 2005). At Lucky Strike, a vent field located south of the Azores on the Mid-Atlantic Ridge (MAR), the deposits are composed largely of a suite of hydrothermal minerals (pyrite, chalcopyrite, sphalerite, marcasite, anhydrite, and amorphous silica) that are typical for basalt-hosted seafloor hydrothermal deposits (Fouquet et al., 1993; Kase et al., 1990; Langmuir et al., 1997; Petersen et al., 2000). However, the deposits at Lucky Strike also contain abundant barite, which Langmuir et al. (1997) link to an enriched mid-ocean basalt (E-MORB) substrate associated with the nearby Azores hotspot.

The mineralogy and distribution of major and trace metals within the Lucky Strike hydrothermal deposits are not uniform, suggesting vent field scale variations in vent fluid composition (Bogdanov et al., 2006; Chavagnac et al., 2018). Both spatial and temporal variations in fluid chlorinity and CO_2 concentrations have been documented, indicating subseafloor fluid phase separation and effects of magma replenishment, respectively (Chavagnac et al., 2018; Von Damm et al., 1998; Langmuir et al., 1997; Pester et al., 2012). Results from previous sulfur isotope analyses from the main field at Lucky Strike indicate typical $\delta^{34}S$ values for mid-ocean ridge hosted hydrothermal systems of between ~0 and 10‰ (Rouxel et al., 2004). In this study, we present new mineralogical, bulk geochemical, and *in situ* sulfur isotope data from hydrothermal samples (n=23) collected during the 2011-2015 MoMARsat maintenance cruises of the EMSO-Azores observatory (European Multidisciplinary Seafloor and water-column Observatory) from several of the hydrothermal edifices at Lucky Strike (Blandin et al., 2013; Cannat et al., 2011; Cannat & Sarradin, 2012; Sarradin & Cannat, 2014, 2015). We document the spatial variations in composition (mineralogical, geochemical, and in S isotopes) of the hydrothermal deposits to 1) evaluate the mineralogical controls on minor and trace element partitioning within the deposits; and 2) link these variations to the geological controls on hydrothermal venting conditions at the vent field scale.

In this study we also further investigate the influence of the Azores hotspot on the composition of hydrothermal deposits along the MAR. We develop geochemical criteria based on major and trace element compositions of hydrothermal deposits from MAR-hosted vent fields to fingerprint specific host rock compositions, which can vary from E-MORB to ultramafic rock.

Insights into the local and regional geological controls on the compositions of seafloor hydrothermal deposits is becoming increasingly important due to the growing interest in the economic potential of these deposits. Large seafloor hydrothermal deposits with high concentrations of base and precious metals (e.g., Cu, Zn, Au, and Ag) are potential targets for future mining (Hannington et al., 2011; Petersen et al., 2016; Rona, 2003). However, environmentally deleterious metals such as As, Cd, Se, Sb, which occur as trace metals within the sulfide minerals can also accumulate (Fallon et al., 2019; Hannington et al., 1999; Layton-Matthews et al., 2008; Martin et al., 2019). Results from this study will contribute to the understanding of the controls of substrate composition on the metal endowment, and therefore provide a framework for predictive assessment of the economic potential and associated environmental risks of exploiting seafloor massive sulfide deposits (SMS) based on geological setting on mid-ocean ridges.

2. Geological setting

The Lucky Strike segment is located along the slow-spreading Mid-Atlantic Ridge, approximately 360 km southwest of the Azores archipelago, near the triple junction between the North American, African, and Eurasian plates (Figure 1) (Cannat et al., 1999; Escartín et al., 2001). This segment is currently spreading at a full rate of ~20-25 mm/yr (Argus et al., 2011; Cannat et al., 1999), and is bound to the north by a non-transform offset with the Menez Gwen segment and to the south by a non-transform offset with the North Famous segment (Figure 1). The Lucky Strike segment formed as a product of rifting of an oceanic plateau associated with the Azores hotspot that began at ~10 Ma (Cannat et al., 1999; Escartín et al., 2001; Gente et al., 2003). The melt anomaly associated with the Azores hotspot is propagating southward, along the ridge, forming a V-shaped ridge that indicates shallowing of the ridges and its flanks towards the Azores hotspot, which is interpreted based on gravity and bathymetric data as a temporal and spatial variations in melt supply to the ridge axis that result from ridge-hotspot interactions (Cannat et al., 1999; Escartín et al., 2001).

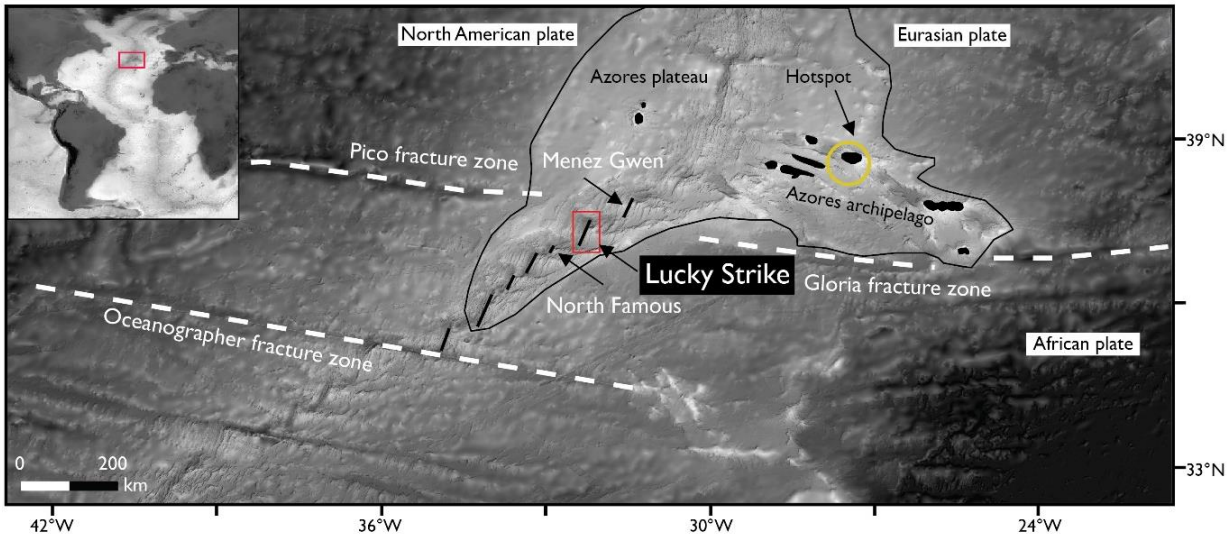

Figure 1. Location of the Lucky Strike segment on the Mid-Atlantic Ridge and its geotectonic context. The black outline highlights the bathymetric high of the Azores plateau and the yellow circle is the location of the Azores hotspot (Gente et al., 2003).

The Lucky Strike segment is ~70 km long, with a prominent axial volcano, named the Lucky Strike Seamount, that rises to 1500 mbsl in the central part of the segment from bathymetric lows of ~3500 mbsl towards the northern end of the segment and ~3200 mbsl towards the southern end of the segment, and is bounded by an overall ~20 km wide fault-bounded rift valley (Figure 2). Bathymetry and sidescan sonar imagery record cyclic volcanic (magmatic) crustal construction

followed by tectonic (rifting) phases (Escartín et al., 2014). Recent volcanic episodes produced two volcanic centers that are aligned along the ridge axis and separated by a flat depression that is interpreted to be a recent but now fossil lava lake (Figure 3a) (Humphris et al., 2002; Ondréas et al., 2009). Both volcanic structures are now cut by a series of ridge-parallel normal faults, with the older, northern, volcanic edifice experiencing a higher degree of rifting than the younger, southern, volcanic edifice (Figure 3a) (Escartín et al., 2014; Humphris et al., 2002). The Lucky Strike rift valley floor is paved by volcanic rocks that range in composition from transitional mid-ocean ridge basalt (T-MORB) to E-MORB (Gale et al., 2011). Basalts with a more E-MORB affinity are found towards the center of the segment, whereas the T-MORB compositions are distributed along the rest of the segment. The stratigraphy of the lava flows indicate that E-MORB lavas are crosscut by T-MORB lavas (Gale et al., 2011; Langmuir et al., 1997). Lava morphologies vary from sheeted flows to pillow lavas, with sheeted flows dominant in the neovolcanic zone that hosts the hydrothermal fields (Escartín et al., 2014; Gini et al. 2021).

Focused hydrothermal activity is restricted to the central region of the Lucky Strike Seamount (Figure 3). Seismic reflection studies have identified an axial magma chamber that lies ~3.5 km below the seafloor, and normal faults that propagate below the axial volcano (Combier et al., 2015; Singh et al., 2006). Microseismicity data suggest that hydrothermal circulation occurs primarily along-axis, and extends into the crust to within a few hundred meters of the axial magma chamber reflector in the narrow faulted area at the volcano summit (Crawford et al., 2013). The location of the vent field is also associated with a crustal magnetic low caused by hydrothermal alteration of the underlying rocks (Miranda et al., 2005).

At the vent field scale venting and hydrothermal deposits are associated with normal faults and occur for the most part near a fossil lava lake at the volcano summit (Figure 3) (Barreyre et al., 2012; Escartín et al., 2015; Fouquet et al., 1994; Ondréas et al., 2009). Focused venting also occurs 1.4 km to the east of the central ridge axis, at a site called Capelinhos (Escartín et al., 2015). The spatial association of hydrothermal venting with faulting suggest that faulting is the primary control on fluid discharge (Barreyre et al., 2012; Escartín et al., 2015). Diffuse venting has been documented at Ewan, located 1.5 km south of the main field (Figure 3) (Escartín et al., 2015). The maximum temperature measured is 340°C at the main Lucky Strike field (South Crystal) and 324°C at Capelinhos (Barreyre et al., 2014; Chavagnac et al., 2018). The hydrothermal deposits at Lucky Strike were identified in previous studies via dredging, followed by autonomous underwater vehicle (AUV) and remotely operated vehicle (ROV) bathymetric mapping coupled with photomosaic imaging (Barreyre et al., 2012; Escartín et al., 2015; Langmuir et al., 1997; Langmuir et al., 1992; Ondréas et al., 2009). Observations from time series imaging of the seafloor, acquired in 1996, 2006, 2008, and 2009, suggest that the heat flux associated with hydrothermal venting is decreasing, likely as a result of cooling of the axial magma chamber that is driving the fluid circulation in this system (Thibaut Barreyre et al., 2012). Radioisotope (^{226}Ra) dating of hydrothermal barite indicates that hydrothermal venting at this site has been ongoing for at least 6,600 years and has accumulated at an average rate of ~194 t/yr (Sánchez-Mora et al., submitted).

Rock samples for this study were collected using the Victor 6000 ROV during the MoMARsat cruises from 2011 to 2015 on the R/V *Pourquoi pas ?* and R/V *Thalassa* in 2012. Sampling mainly focused on hydrothermal deposits on several sites within the main vent field as well as on Capelinhos (Table 1). Samples for the main field at Lucky Strike (n=19) and Capelinhos (n=4)

range from sulfide blocks at the bases of hydrothermal edifices to active and inactive sulfide-rich chimneys and samples that precipitated on temperature probes (Table 1).

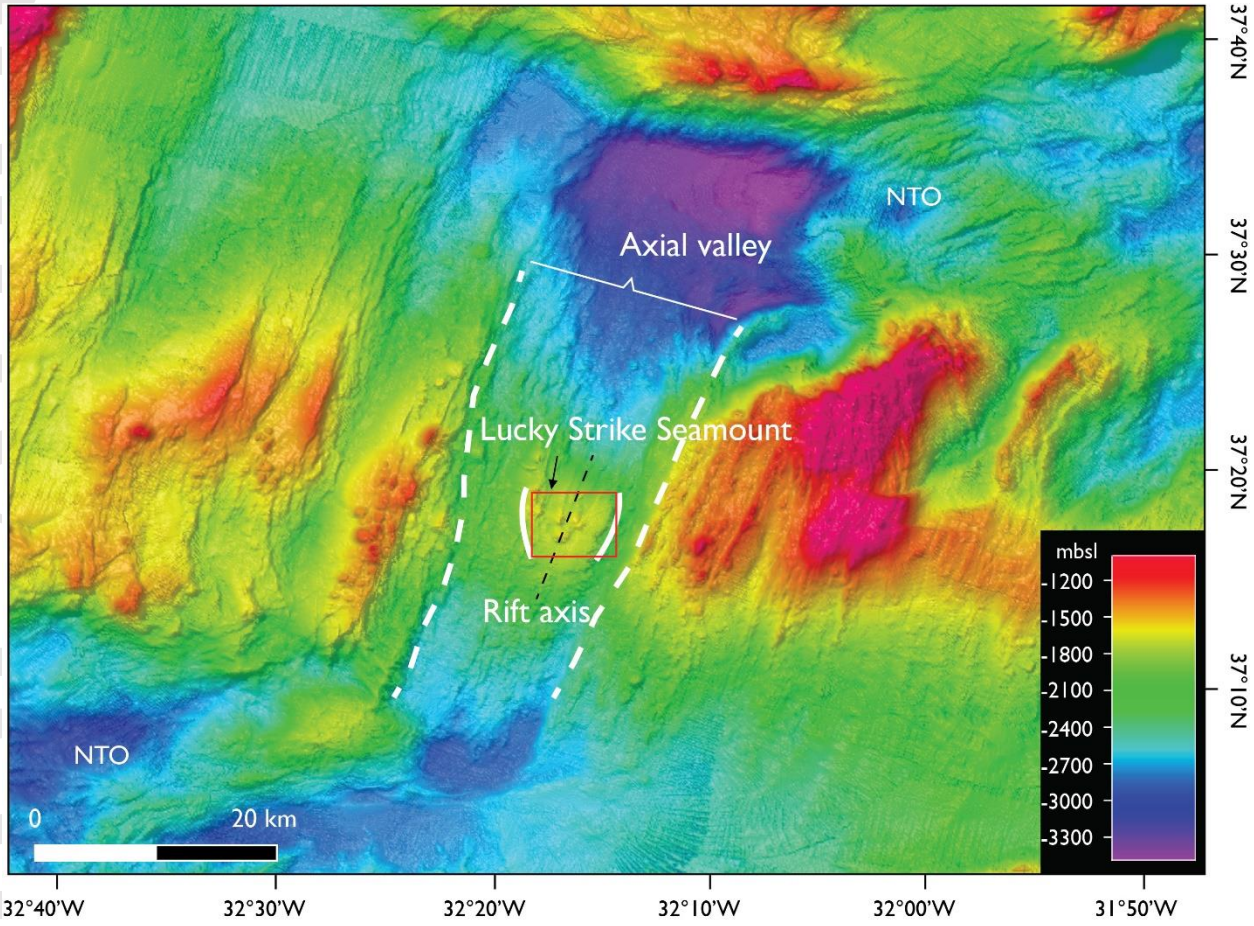

Figure 2. Segment scale bathymetric map of Lucky Strike (~40 m resolution). Red rectangle shows the area of study (Figure 3a). White solid lines show approximate extent of the Lucky Strike Seamount. The white dashed lines are the axial valley walls. NTO are non-transform offsets. Bathymetry from the Sudaçores cruise (Cannat et al., 1999; Escartín et al., 2001).

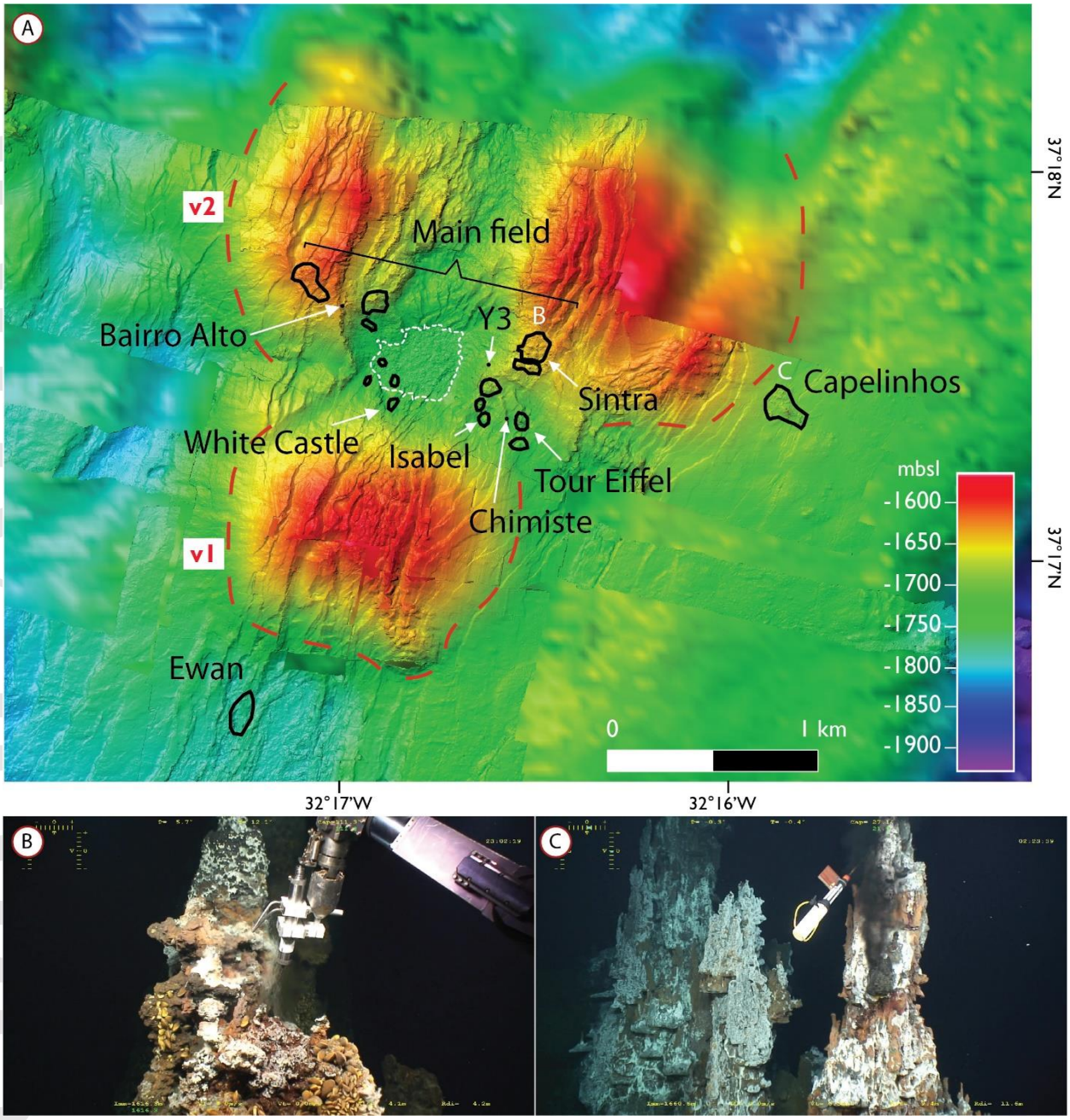

Figure 3. A) Outlines of the main hydrothermal areas from the Lucky Strike hydrothermal system. High temperature venting of 340°C (T_{max}) occurs at the main Lucky Strike hydrothermal field and 324°C fluid (T_{max}) at Capelinhos. Ewan is a site of diffuse venting (Barreyre et al., 2014; Escartín et al., 2015). The dashed red lines show the volcanic rifted structures v2 (higher degree of rifting) to the north and v1 in the south. White dashed outline is a fossil lava lake. B) Venting of 222°C fluid (T_{max});(Von Damm et al., 1998) at a sulfide chimney at the Sintra vent complex within the main Lucky Strike hydrothermal field. The length of the robotic arm is ~75 cm. C) Chimneys and high-temperature venting at the Capelinhos site (Chavagnac et al., 2018). The temperature probe is ~1 m long. Bathymetry sources: Ondréas et al. (2009) and Escartín et al. (2015).

3. Methodology

3.1. Bulk geochemistry

For bulk multi-element geochemistry, 23 samples were crushed at Memorial University using a ring pulverizer with a tungsten carbide grinding container and then analyzed at Activation Laboratories LTD (Actlabs). Samples were analyzed using: 1) instrumental neutron activation analysis (INAA) for Au, Ag, As, Ba, Co, Fe, Na, Sb, Se, and Zn; and 2) Na_2O_2 fusion and inductively coupled plasma optical emission spectroscopy (ICP-OES) and mass spectrometry (ICP-MS) for Ca, Mo, Ni, Sr, Al, Cd, Cu, Ga, Ge, In, Mg, Mn, Pb, S, Si, Sn, Tl, and V (Hoffman, 1992). Accuracy and precision for INAA values are both better than ±5%, based on repeat (n=7) analysis of the GXR-1 standard. For the Na_2O_2 fusion ICP method, accuracy is better than ±7%, based on repeat (n=3) measurement of the OREAS 922 standard, with the exceptions of Ni and Sr, for which accuracy is 17%. Precision for the ICP method is better than 10%, except for Ni and Pb, which have precisions of 20% and 12%, respectively.

3.2. *In situ* sulfur isotope measurements

In situ sulfur isotope measurements were performed using a Cameca IMS 4f Secondary Ion Mass Spectrometer at the MAF-IIC Microanalysis Facility at Memorial University. Sulfide-bearing samples (n=16) were embedded in epoxy in a 25.4 mm diameter aluminum ring and prepared as polished mounts, and sputter coated with 300 Å of Au to mitigate charging under primary ion bombardment. Isotopic analyses (n=52) were performed by bombarding the sample with a 0.8-1.0 nA primary ion microbeam accelerated through a 10 keV potential and focused into a 15-20 µm diameter spot. Each spot was pre-sputtered for 120 s using a 10 µm raster to exclude exotic material in the polished surface from the analysis. Negatively charged sputtered secondary ions were accelerated into the mass spectrometer through a 4.5 keV potential. Signals for $^{32}S^-$, $^{34}S^-$ and a background position at 31.67 Da were obtained by cyclical magnetic peak switching. Standard counting time and peak sequence used were 0.5 s at the background position, 2.0 s on $^{32}S^-$, and 6.0 s on $^{34}S^-$. A typical analysis consisted of accumulating 80 peak cycles. All peak signals were collected with an ETP 133H multiple-dynode electron multiplier (em) and processed through ECL-based pulse-counting electronics with an overall dead time of 11 ns. The production and detection of sputtered secondary ions produces an instrumental mass fractionation (IMF) bias between the actual $^{34}S/^{32}S$ of the sample and that measured by the mass spectrometer. The magnitude of the IMF varies substantially between sulfide minerals. For this reason, the $^{34}S/^{32}S$ measured in samples of pyrite were corrected for IMF by comparison to replicate measurements of in-house reference materials UL9B (pyrite; $\delta^{34}S$: +16.3‰) and a Norilsk chalcopyrite ($\delta^{34}S$: +8.4‰). Measured $^{34}S/^{32}S$ ratios are transformed to the Vienna Cañon Diablo Troilite (V-CDT) scale using $^{34}S/^{32}S_{VCDT}$ = 0.0441626 (Ding et al., 2001). Data are presented in standard delta notation:

$$\delta^{34}S = \left(\frac{(R)_{sample}}{(R)_{V-CDT}} - 1\right) \times 1000$$

Where R = $^{34}S/^{32}S$. Analyses yield internal precisions on individual $\delta^{34}S$ determinations of better than ±0.3‰ (1σ) and the overall reproducibility, based on replicate standards analyses, is typically better than ±0.45‰ (1σ).

4. Results

4.1. Mineralogy and geochemistry

4.1.1.Mineralogy

Rock samples from Lucky Strike were collected primarily from the hydrothermally active Sintra, Tour Eiffel, Chimiste, Isabel, White Castle and Bairro Alto edifices (Figure 3a; Ondréas et al., 2009). Within the samples, mineral distributions change from the exterior to the interior of the chimneys, as typically described at black smoker deposits (Fouquet et al., 2010; Hannington et al., 1995; Haymon, 1983), with a lower temperature mineral assemblage of barite, anhydrite, marcasite, and pyrite with millimeter-scale goethite rims dominating the exterior of the chimney, and a higher-temperature mineral assemblage of sphalerite and chalcopyrite dominating the interior and lining fluid conduits (Figure 4a-e). Early marcasite forms plumose, colloform, or ring-like textures. Later stage marcasite is massive and euhedral. Subhedral to euhedral pyrite overgrows marcasite and co-precipitates with sphalerite that exhibits a range of textures, from plumose to subhedral and massive (Fig. 4d, f, g). Late stage chalcopyrite has massive and euhedral textures, and is often replacing or overgrowing sphalerite (Fig. 4d, h, i). Supergene alteration consists of exterior goethite rinds and atacamite (Figure 4f), and secondary covellite and bornite replacing chalcopyrite (Figure 4g). No major mineralogical differences are identified between Sintra, Tour Eiffel, and White Castle, except for an absence of pyrite in samples collected from Sintra, and absence of covellite in samples from White Castle.

Samples from Capelinhos show similar mineralogical assemblages and textural characteristics to the main Lucky Strike field, with lower temperature assemblages in the outer chimney walls that transition to higher temperature assemblages towards the interior. However, the primary difference is the occurrence of a second generation of sphalerite (Sph2), chalcopyrite (Cpy2), and barite (Ba2), that overprint previous generations (Figure 4g, h, i) suggesting temporal fluctuations in temperature of mineralizing fluids (Eldridge et al., 1983). Supergene alteration includes replacement of chalcopyrite by covellite and minor bornite, goethite and atacamite.

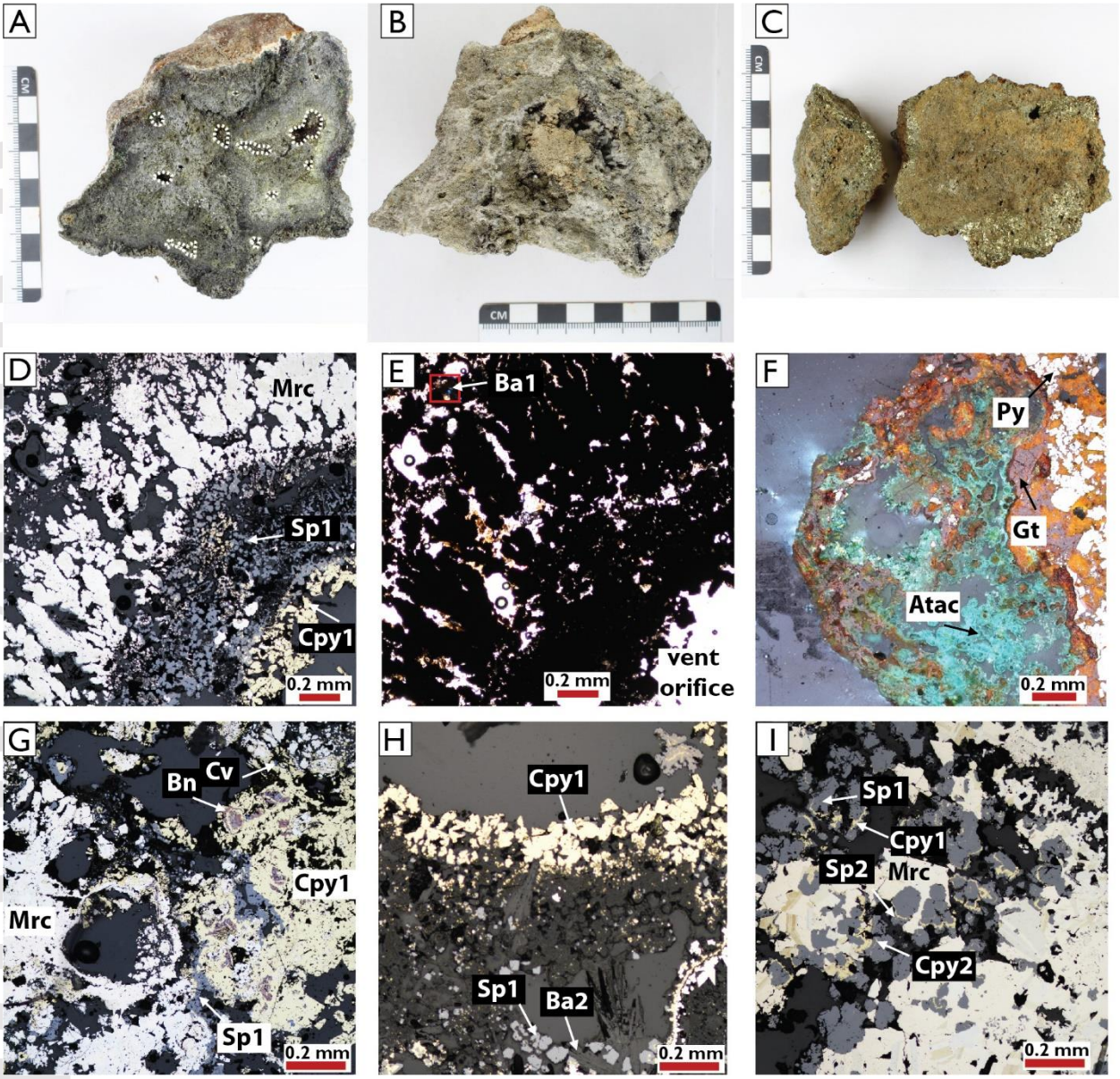

Figure 4. The main mineral assemblages of hydrothermal deposits at Lucky Strike. A) Typical chimney sample from Tour Eiffel (MOM14-579-ROC1) with sulfate and Fe-sulfide minerals dominating the exterior, and chalcopyrite and sphalerite in the interior, and lining the open fluid conduits (in white dashed lines). B) Sample collected from the side of the Sintra (MOM12-502-ROC1) edifice, with abundant barite, anhydrite, marcasite, and sphalerite. C) Chimney fragment from Tour Eiffel (MOM13-532-ROC2), dominated by marcasite and chalcopyrite. D) Typical mineralogical transition, from barite and marcasite towards the exterior, to sphalerite and chalcopyrite lining an interior high-temperature fluid conduit. Sample from the Tour Eiffel site (MOM14-579-ROC1). E) The same photomicrograph as D but under transmitted, crossed polarized light. F) Supergene alteration consisting of atacamite and goethite occurring on outer chimney walls. Sample from the Chimiste site (MOM15-PL607_ROC3). G) Supergene alteration, with minor bornite and covellite replacing chalcopyrite. Sample from the Capelinhos site (MOM14-PL583-ROC4). H) Sphalerite overgrown by chalcopyrite in a vent orifice and a second

generation of acicular barite infilling voids. Sample from the inner part of a chimney from Tour Eiffel (MOM14-579-ROC1). I) Sphalerite and chalcopyrite overgrown by a second generation of sphalerite and chalcopyrite and marcasite from the Capelinhos site (MOM14-PL583-ROC4). Images D, G, H, and I are plane-polarized reflected light photomicrographs. Image F was taken under cross-polarized reflected light.

4.1.2.Bulk geochemistry of hydrothermal deposits

Table 1 summarizes 28-element geochemical analysis of 19 sulfide-rich samples from Lucky Strike and sulfide-rich hydrothermal precipitates on the temperature probes. Notable results from the chimney samples include average base metal concentrations of 7.2 wt.% Cu, with a range of 0.012-26.4 wt.% Cu, 5.9 wt.% Zn, with a range of 0.037-37.4 wt.% Zn, 6.5 wt.% Ba, with a range of 0.027-44.4 wt.% Ba, and 630 ppb Au, with a range of 8-2030 ppb Au. Additionally, concentrations of Sr of up to 5940 ppm, Mo of up to 351 ppm, and Se with of up to 2570 ppm. Rare earth element concentrations are generally below detection limits. There are no significant elemental enrichments or depletions associated with the different vent sites at Lucky Strike. The composition of the temperature probe precipitates have notably lower concentrations of Zn, Pb, Ba, Au, and Ag.

Principal component analysis (PCA) was performed to identify statistical trends in the chimney sample dataset. The analysis was performed using the 28 elements of which at least 50% of the samples contained concentrations greater than their respective detection limits. When reported concentrations were below detection limits, a value representing 65% of the detection limit was used (Palarea-Albaladejo et al., 2014). A sensitivity analysis using different thresholds for percentages of samples below detection limit and different values to represent the analyses below detection limit resulted in negligible changes to the results of the PCA analysis. A centred-log-ratio transformation was applied to the raw data to avoid closure problems and spurious correlations (Pawlowsky-Glahn & Egozcue, 2006). The centred-log-ratio transformation (clr(x)) was calculated using the following equation:

$$\mathrm{clr}(\boldsymbol{x}) = [ln(x_1/(x_1 \cdot x_2 \ldots x_D))^{1/D}) , ln(x_2/(x_1 \cdot x_2 \ldots x_D))^{1/D}), \ldots, ln(x_D/(x_1 \cdot x_2 \ldots x_D)^{1/D})]$$

where D = the number of samples.

The PCA (Figure 5) reveals a cluster of elements associated with high-temperature sulfide minerals (e.g., Co, Cu, Se and Sn) with a negative PC1 loading, and a second cluster of elements associated with lower-temperature sulfide minerals (Ga, Sb, Zn, Cd, Mn, Si) with a positive PC1 loading. Principal component 2 has positive loadings for sulfide mineral associated elements (transition and post-transition metals), and negative loadings for sulfate and oxide minerals associated elements (alkaline earth metals such as Ba, Sr, Ca, and Mg) but also Ni. Principal component 1 accounts for 37% of the variability in the dataset and PC2 accounts for 17% of the variability.

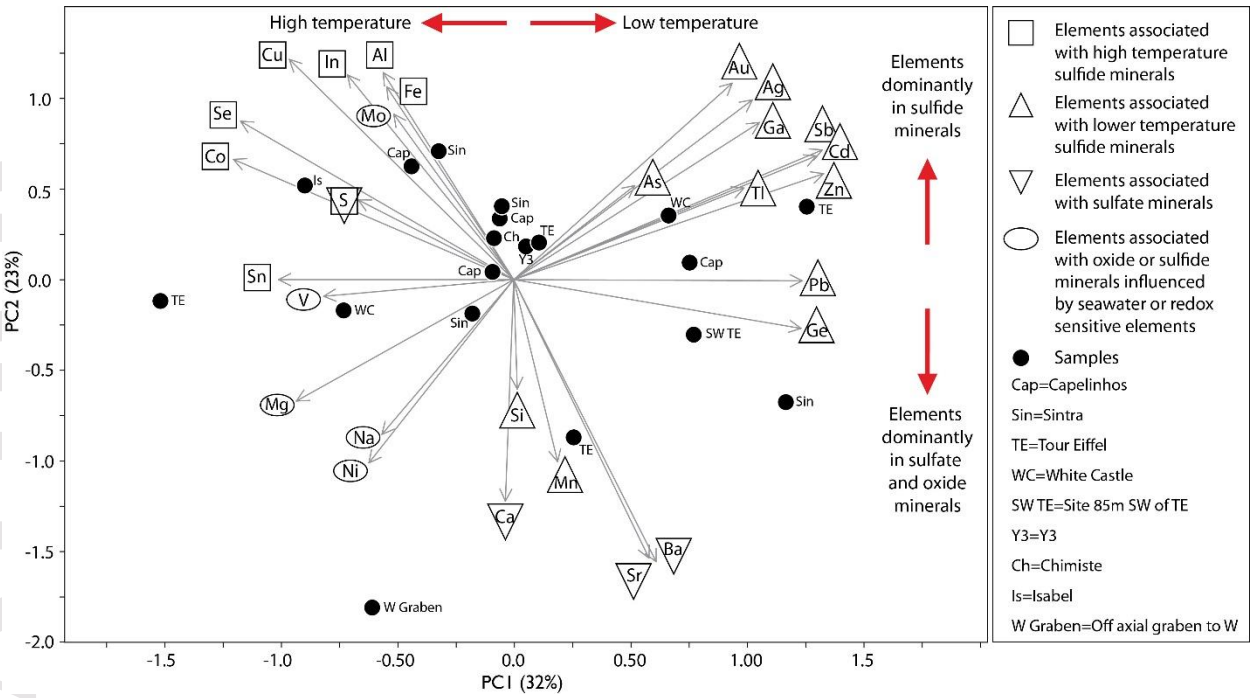

Figure 5. Principal component analysis of bulk rock geochemistry (black dots) from the main Lucky Strike and Capelinhos hydrothermal sites. Elements in squares are associated with high temperature sulfide minerals; elements in upright triangles are associated with lower temperature sulfide minerals; elements in inverted triangles are associated with sulfate minerals; elements in ovals are associated with seawater or redox sensitive (Mo, V, and Ni).

Table 1. Chemical composition of hydrothermal samples from Lucky Strike vent field (see supporting information Table S1 for full dataset that includes additional elements that were largely below detection limit).

Analyte Symbol	Latitude	Longitude	Description	IGSN	Cu (wt.%)	Zn (wt.%)	Pb (ppm)	Fe (wt.%)	S (wt.%)	Si (wt.%)	Al (wt.%)	Ca (wt.%)	Na (wt.%)	Mg (wt.%)	Ba (ppm)	Sr (ppm)	Mo (ppm)
Detection Limit					0.0002	0.001	0.8	0.01	0.01	0.01	0.01	0.01	0.001	0.01	20	3	1
Analysis Method					FUS	INAA	FUS	INAA	FUS	FUS	FUS	FUS	INAA	FUS	INAA	FUS	FUS
Capelinhos (1678 mbsl)																	
MOM14-583-ROC1-S	37.28973	-32.281042	Block from the base of Capelinhos edifice	CNRS0000007069	5.4	1.01	113	21.8	27	11.9	0.04	0.09	0.12	<0.01	45200	1150	33
MOM14-PL583-ROC4	37.289418	-32.263983	Fragment A of active chimney	CNRS0000007072	5.09	2.49	193	42.4	50.1	0.04	0.03	0.48	0.08	<0.01	1760	97	37
MOM14-PL583-ROC4	37.289418	-32.263983	Fragment B of active chimney	CNRS0000007072	11.4	1.53	137	40	45.3	0.22	0.11	0.05	0.22	<0.01	330	20	40
MOM13-528-ROC1-S	37.289467	-32.263972	Block from the base of Capelinhos edifice	N/A	0.0459	6.64	716	35.4	46.9	0.17	0.05	0.07	0.16	0.01	12900	737	69
Y3 (1730 mbsl)																	
MOM11-454-ROC7	37.291867	-32.277817	Base of small active chimney	CNRS0000007017	4.02	7.57	489	31.5	41.5	1.56	0.5	0.19	0.3	0.02	19300	850	318
White Castle (1705 mbsl)																	
MOM15-603-ROC5	37.28973	-32.281042	Block from active edifice	CNRS0000007099	1.41	27.6	887	12.3	34.7	2.94	0.64	0.07	0.25	0.03	4960	239	121
MOM15-603-ROC6	37.28973	-32.281042	Block from active edifice	CNRS0000007100	10.1	0.614	209	27.3	35.8	5.45	0.36	0.1	0.18	0.04	38300	1700	351
Off axial graben to the W (1612 mbsl)																	
MOM15-605-ROC2	37.295229	-32.284963	From inactive site	CNRS0000007103	0.035	0.048	31.3	0.56	6.29	0.6	<0.01	0.16	0.12	0.02	444000	5940	7
Tour Eiffel (1696 mbsl)																	
MOM11-457-ROC8	37.289033	-32.275667	Small inactive chimney W of Tour Eiffel	CNRS0000007018	1.52	37.4	823	17.5	38.5	0.95	0.08	0.1	0.06	<0.01	34500	1040	59
MOM14-579-ROC1	37.290722	-32.281038	Small inactive chimney	CNRS0000007062	7.36	7.62	454	28.5	36.7	5.36	0.61	0.1	0.19	0.01	23800	667	167
MOM13-532-ROC1	37.288933	-32.275417	Block in the E slope of Tour Eiffel		0.012	0.128	746	26.3	33.2	4.63	<0.01	0.1	0.14	<0.01	99400	2080	25
MOM13-532-ROC2	37.288933	-32.275417	Block of sulfide at base of Tour Eiffel	N/A	19.4	0.037	19.9	31.7	41.3	0.51	0.18	0.07	0.28	0.05	950	48	22
Site 85 m SW of Tour Eiffel (1691 mbsl)																	

MOM12-504-ROC1	37.288583	-32.276333	Block in inactive area 85 m SW of Tour Eiffel	CNRS0000007053	1.02	10.8	502	11.2	17.7	13.6	0.28	0.15	0.38	0.03	112000	1420	66
Sintra (1630 mbsl)																	
MOM11-452-ROC1	37.292083	-32.274717	Small inactive chimney on sulfide-rich basement at the base of Sintra	CNRS0000007011	2.45	0.554	993	38.8	38.1	0.91	0.15	0.84	0.41	0.11	14200	407	67
MOM11-452-ROC2	37.292083	-32.2747	Fragments of inactive chimney	CNRS0000007012	25.6	0.593	379	31.9	37.4	0.32	0.15	0.04	0.21	0.02	310	24	100
MOM11-452-ROC3	37.292033	-32.274717	Fragments of inactive chimney	CNRS0000007013	26.4	1.57	306	26.7	33.5	1.77	0.26	0.06	0.21	0.03	2870	41	59
MOM12-502-ROC1	37.292167	-32.2750	Active chimney	CNRS0000007051	0.036	5.08	541	4.74	9.41	0.3	<0.01	0.17	0.29	<0.01	381000	5110	11
Isabel (1703 mbsl)																	
MOM15-PL607_ROC5	37.28912	-32.277405	Sulfide block	CNRS0000007108	13.5	0.22	177	35.1	40.3	0.51	0.23	0.05	0.23	0.03	380	23	267
Chimiste (1687 mbsl)																	
MOM15-PL607_ROC3	37.289291	-32.276545	Sulfide block	CNRS0000007106	1.27	0.562	354	30.3	38.6	12.3	0.19	0.04	0.2	<0.01	270	20	69
Temperature probe precipitates																	
Cyprès (1740 mbsl)																	
MOM14-HN29008-ROCK	37.290787	-32.280972	Precipitate on temperature probe	N/A	8.5	0.049	8.1	44.3	48.5	0.08	0.03	0.34	0.05	0.02	<20	36	6
Crystal (1730 mbsl)																	
HT010-CR12	37.29088	-32.28202	Precipitate on temperature probe	N/A	2.41	2.12	230	10.3	29.2	0.42	0.17	17.4	0.21	0.07	7420	2100	444
Cimendef (1702 mbsl)																	
MOM14-HT007-ROCK	37.288083	-32.275838	Precipitate on temperature probe	N/A	5.25	0.098	18.2	44.8	50.8	0.22	0.09	1	0.07	0.04	560	132	11
Y3 (1730 mbsl)																	
LS-BS-WHOI	37.29187	-32.27785	Precipitate on temperature probe	N/A	15.2	2.13	201	30.1	35.6	3.27	0.24	0.13	0.1	<0.01	32300	1360	212

FUS = analysis by ICP-OES or ICP-MS, with samples prepared by fusion with a Na_2O_2 flux
INAA = analysis by instrumental neutron activation

Table 1. *(continued)* Chemical composition of hydrothermal samples from Lucky Strike vent field (see supporting information Table S1 for full dataset that includes additional elements that were largely below detection limit).

Analyte Symbol	V (ppm)	Ni (ppm)	Co (ppm)	Se (ppm)	Au (ppb)	Ag (ppm)	As (ppm)	Ga (ppm)	Ge (ppm)	Sb (ppm)	Cd (ppm)	Tl (ppm)	In (ppm)	Sn (ppm)	Mn (ppm)
Detection Limit	5	10	0.1	0.5	2	2	1	0.2	0.7	0.1	2	0.1	0.2	0.5	3
Analysis Method	FUS	FUS	INAA	INAA	INAA	INAA	INAA	FUS	FUS	INAA	FUS	FUS	FUS	FUS	FUS
Capelinhos (1678 mbsl)															
MOM14-583-ROC1-S	<5	<10	277	<0.5	258	22	128	27.5	6.8	11.4	43	5.4	10.1	3.7	55
MOM14-PL583-ROC4	<5	10	158	131	256	21	291	27.4	14.8	15	55	16.2	2.6	5.3	76
MOM14-PL583-ROC4	9	10	258	150	237	22	229	15	10.8	11.4	30	5.5	6	3.3	38
MOM13-528-ROC1-S	<5	10	14.1	<0.5	323	39	236	51.4	22.8	49.9	213	61.9	1	1	91
Y3 (1730 mbsl)															
MOM11-454-ROC7	110	10	337	127	625	88	307	45.8	33.2	23.7	288	44	1.4	2.5	634
White Castle (1705 mbsl)															
MOM15-603-ROC5	<5	<10	64.6	42.6	748	152	277	63.8	60.8	50	1250	27.6	0.7	3.5	464
MOM15-603-ROC6	51	30	604	237	205	9	142	8.2	21.9	5	17	10.7	3.4	2.3	193
Off axial graben to the W (1612 mbsl)															
MOM15-605-ROC2	6	10	7.4	<0.5	8	<2	14	1.1	3.4	0.8	<2	<0.1	<0.2	1.7	369
Tour Eiffel (1696 mbsl)															
MOM11-457-ROC8	6	10	33	<0.5	2030	278	346	354	68.2	166	1700	42.6	5.7	1.1	424
MOM14-579-ROC1	122	40	107	179	724	76	387	62.6	29.8	36.9	288	38.5	4.2	2.3	349
MOM13-532-ROC1	<5	20	48.5	<0.5	309	<2	449	1.7	23.1	2.3	4	151	<0.2	1	205
MOM13-532-ROC2	12	10	167	2570	73	<2	99	1.7	5.7	1.6	<2	1.2	2.5	6.3	60
Site 85 m SW of Tour Eiffel (1691 mbsl)															
MOM12-504-ROC1	35	20	50.6	<0.5	1750	165	642	55.3	43	82.8	291	21.6	0.6	0.6	1240
Sintra (1630 mbsl)															
MOM11-452-ROC1	131	20	467	69.9	1340	49	635	46.5	19.9	39	9	23.4	12.7	1.1	1830
MOM11-452-ROC2	20	10	225	346	1010	94	223	36.5	19.5	19	25	6.5	10.5	4.2	113
MOM11-452-ROC3	16	10	47.5	106	677	59	242	28	24.1	28	59	13.4	6.9	1.6	153
MOM12-502-ROC1	<5	<10	8.5	<0.5	369	89	168	10.4	50.9	29.5	98	36.9	<0.2	0.9	65

Isabel (1703 mbsl)															
MOM15-PL607_ROC5	44	10	409	907	539	44	268	5.1	6.9	6.3	6	9.8	6.3	5.9	211
Chimiste (1687 mbsl)															
MOM15-PL607_ROC3	<5	20	89.2	28.9	496	59	477	3.4	8.1	9.6	27	18.4	0.3	1	353
Temperature probe precipitates															
Cyprès (1740 mbsl)															
MOM14-HN29008-ROCK	<5	60	559	227	37	6	85	0.7	5.1	0.5	<2	<0.1	8.4	17.7	11
Crystal (1730 mbsl)															
HT010-CR12	57	1450	101	70.6	189	28	97	12.2	9.7	12.4	122	9.2	2.5	3	92
Cimendef (1702 mbsl)															
MOM14-HT007-ROCK	<5	20	86.8	385	47	<2	96	1.4	5.8	1.1	3	1.3	1.7	2.2	25
Y3 (1730 mbsl)															
LS-BS-WHOI	58	30	198	490	228	52	120	17.8	19.9	8.3	92	21	3.1	2.3	341

Table 2. *In situ* sulfur isotope compositions of marcasite (mrc), pyrite (py), and chalcopyrite (cpy) from Lucky Strike. SEM= standard error of the mean.

	Mineral	Texture	Mineral assemblage	$\delta^{34}S$ (‰)	SEM
Capelinhos site					
MOM14-PL583-ROC4_Cpy1	Cpy	euhedral/massive	marcasite-chalcopyrite	7.7	0.5
MOM14-PL583-ROC4_Cpy3	Cpy	massive	chalcopyrite	6.3	0.2
MOM14-PL583-ROC4_Cpy1	Cpy	massive	chalcopyrite	6.5	0.2
MOM14-PL583-ROC4_Cpy2	Cpy	massive	chalcopyrite	6.5	0.2
MOM14-583-ROC1-S _Cpy1	Cpy	euhedral	marcasite-chalcopyrite	7.2	0.3
MOM14-583-ROC1-S _Cpy2	Cpy	euhedral/massive	marcasite-chalcopyrite	4.7	0.6
MOM13-528-ROC1-S_Cp1	Cpy	cpy disease	sphalerite-chalcopyrite	8.7	0.5
MOM13-528-ROC1-S_Mrc2	Mrc	plumose	marcasite-barite-sphalerite	3.4	0.3
MOM13-528-ROC1-S_Mrc1	Mrc	plumose	marcasite-barite-sphalerite	3.9	0.4
MOM14-583-ROC1-S_Mrc2	Mrc	massive/subhedral	marcasite-chalcopyrite	5.2	0.3
MOM14-583-ROC1-S_Mrc1	Mrc	atoll/ring	marcasite-chalcopyrite	4.0	0.8
MOM14-PL583-ROC4_Mrc1	Mrc	atoll/ring	marcasite	1.7	0.6
MOM14-PL583-ROC4_Mrc2	Mrc	euhedral/massive	marcasite	4.4	0.7
Main Field-Chimiste					
MOM15-PL607_ROC3_Mrc1	Mrc	euhedral	marcasite	-0.5	0.3
Main Field-Isabel					
MOM15-PL607_11_ROC5_Cpy1	Cpy	massive	marcasite-chalcopyrite	2.8	0.2
MOM15-PL607_11_ROC5_Cpy2	Cpy	euhedral	marcasite-chalcopyrite	2.8	0.5
MOM15-PL607_11_ROC5_Mrc1	Mrc	colloform	marcasite-chalcopyrite	-2.4	0.3
MOM15-PL607_11_ROC5_Mrc2	Mrc	plumose	marcasite-chalcopyrite	-0.7	0.4
Main Field-Sintra					
MOM11-452-ROC3_Cpy2	Cpy	euhedral/massive	chalcopyrite-sphalerite	2.0	0.3
MOM11-452-ROC3_Cpy1	Cpy	euhedral/massive	chalcopyrite-sphalerite	3.3	0.4
MOM11-452-ROC3_Cpy3	Cpy	euhedral/massive	chalcopyrite	2.1	0.3
MOM11-452-ROC2_Cpy2	Cpy	massive	chalcopyrite-marcasite-covellite	4.7	0.4
MOM11-452-ROC2_Cpy1	Cpy	massive	chalcopyrite-marcasite-covellite	6.0	0.4
MOM11-452-ROC3_Mrc1	Mrc	atoll/ring	marcasite-chalcopyrite	-0.7	0.3
MOM11-452-ROC1_Mrc2	Mrc	colloform	marcasite-barite	-0.6	0.4
MOM12-502-ROC1_Mrc1	Mrc	colloform	marcasite-barite	1.1	0.5
MOM11-452-ROC1_Mrc1	Mrc	colloform	marcasite-barite	1.1	0.6
MOM11-452-ROC2_Mrc1	Mrc	euhedral	marcasite-chalcopyrite	0.9	0.3
Main Field-Tour Eiffel					
MOM13-532-ROC2_Cpy1	Cpy	massive	marcasite-chalcopyrite	4.3	0.3
MOM11-457-ROC8_Cpy1	Cpy	massive	chalcopyrite-sphalerite	4.8	0.3
MOM14-579-ROC1_Cpy3	Cpy	euhedral	chalcopyrite-sphalerite	5.3	0.4
MOM13-532-ROC2_Mrc1	Py	euhedral/massive	marcasite-chalcopyrite	1.6	0.3
MOM12-504-ROC1_Mrc1	Mrc	colloform	barite-marcasite	-0.3	0.6

MOM11-457-ROC8_Mrc1	Mrc	plumose	marcasite-barite	0.1	0.4
MOM13-532-ROC1_Mrc2	Mrc	colloform	marcasite	0.9	0.3
MOM13-532-ROC1_Mrc6	Mrc	colloform	marcasite	0.9	0.3
MOM13-532-ROC1_Mrc4	Mrc	colloform	marcasite	1.0	0.2
MOM13-532-ROC1_Mrc3	Mrc	colloform	marcasite	1.1	0.2
MOM13-532-ROC1_Mrc5	Mrc	colloform	marcasite	1.3	0.3
MOM13-532-ROC1_Mrc7	Mrc	massive	marcasite-sphalerite	1.4	0.5
MOM13-532-ROC1_Mrc1	Mrc	colloform	marcasite	1.5	0.7
MOM14-579-ROC1_Mrc2	Mrc	plumose	barite-marcasite	1.3	0.3
MOM14-579-ROC1_Mrc1	Mrc	atoll/ring	barite-marcasite	2.0	0.3
Main Field-White Castle					
MOM15-603-ROC6_Cpy1	Cpy	euhedral	chalcopyrite-sphalerite	3.1	0.4
MOM15-603-ROC6_Mrc1	Py	euhedral	marcasite	1.5	0.3
Main Field-Y3					
LS-BS-WHOI_Cpy3	Cpy	euhedral	chalcopyrite-sphalerite	1.0	0.3
LS-BS-WHOI_Cpy1	Cpy	euhedral	chalcopyrite-sphalerite	1.8	0.4
LS-BS-WHOI_Cpy2	Cpy	euhedral	chalcopyrite-sphalerite	1.8	0.5
MOM11-454-ROC7_Cpy1	Cpy	euhedral	chalcopyrite-sphalerite	3.7	0.4
LS-BS-WHOI_Mrc1	Mrc	plumose	marcasite-barite	-1.0	0.3
MOM11-454-ROC7_Mrc1	Mrc	plumose	marcasite	-2.5	0.2
MOM11-454-ROC7_Mrc2	Py	plumose/euhedral	marcasite	-0.8	0.3

4.2. *In situ* sulfur isotopes

Table 2 summarizes results from *in situ* sulfur isotope measurements for marcasite and chalcopyrite (Figure 6 and 7). The $\delta^{34}S$ values for marcasite and pyrite (n=30) average 1.0‰ (1σ = 1.8) and vary from -2.5 to 5.2‰. Values for chalcopyrite (n=22) average 4.4‰ (1σ = 2.1) and range from 1.0 to 8.7‰. Notable low (negative) $\delta^{34}S$ values of -2.5 and -2.4‰ where obtained on marcasite from the Y3 and Isabel sites, respectively, which are part of the main field. Average marcasite and chalcopyrite sulfur isotope compositions from the main field (0.3‰, n=24, and 3.3‰, n=15, respectively) are lower than those for Capelinhos (3.7‰, n=6, and 6.8‰, n=7, respectively; Figure 7). Marcasite $\delta^{34}S$ values do not vary significantly as a function of texture at the main field (Figure 6). At both sites, chalcopyrite is, on average, isotopically heavier by ~3‰ than marcasite (Figure 7). There is no apparent correlation between $\delta^{34}S$ values and age for the seventeen samples for which both S isotope and age data are available (Sánchez-Mora et al., submitted).

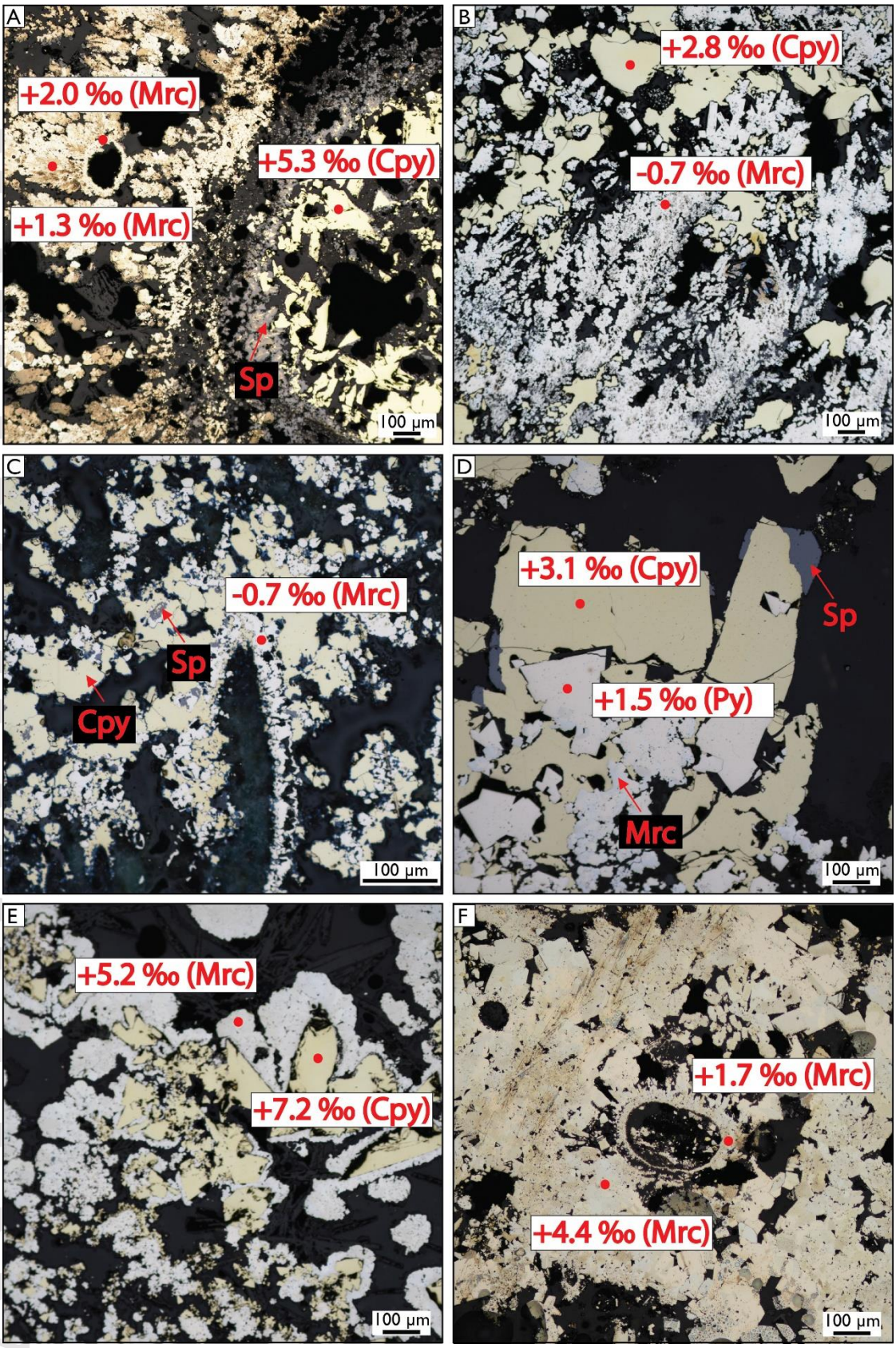

Figure 6. Thin section photomicrographs (plane polarized reflected light) showing locations of $\delta^{34}S$ spot analysis: A) Partially infilled vent orifice with a low-temperature assemblage of atoll-like marcasite with plumose marcasite overgrowths, barite and sphalerite, overprinted by high-temperature euhedral chalcopyrite. Sample from the Tour Eiffel site (MOM14-579-ROC1). B) Plumose marcasite overprinted by euhedral chalcopyrite. Samples from the Isabel site (MOM15-PL607-ROC5). C) Atoll-like marcasite overprinted by massive chalcopyrite. Sample from the Sintra site (MOM11-452-ROC3). D) Euhedral pyrite overprinted by euhedral chalcopyrite. Sample from the White Castle site (MOM15-603-ROC6). E) Anhedral marcasite with later anhedral chalcopyrite infilling. Sample from the Capelinhos site (MOM14-583-ROC1-S). F) Atoll-like marcasite overprinted by massive marcasite. Sample from Capelinhos (MOM14-PL583-ROC4).

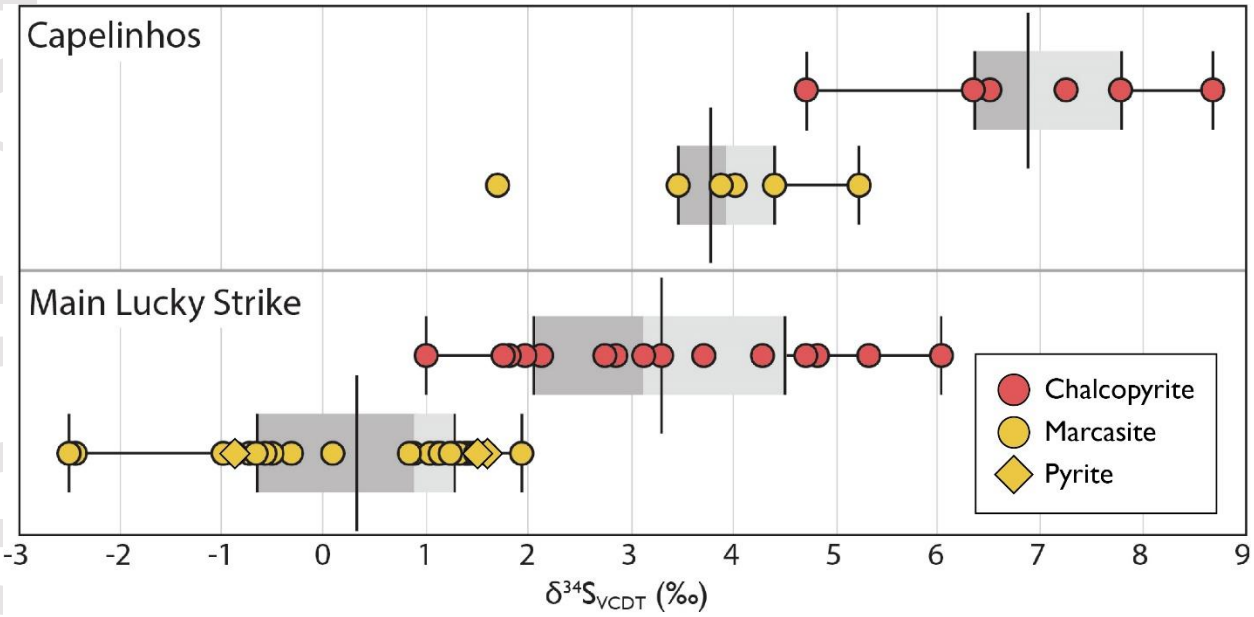

Figure 7. Box plot of *in situ* sulfur isotope $\delta^{34}S$ values for marcasite, pyrite, and chalcopyrite at Lucky Strike, divided by sites. Box and whiskers of quartiles, boxes represent 50% of the data, median is between the boxes, and black line is the average.

5. Discussion

The bulk, minor and trace element geochemical data presented in this study expands on the data originally presented by Bogdanov et al. (2006) by including a more extensive suite of elements such as Au, Ag, As, Ba, Mo, Sb, Se, Sb, Si, and Sn (see Table 1). Additionally, this study includes data from samples from other areas of the vent field not included in the study by Bogdanov et al. (2006), including the Capelinhos site, for which no data has been published to date. Results from the principal component analysis reflect the strong temperature control and influence of seawater on the mineral associations and trace element distributions within the deposits (Figure 5). An analysis of the distribution of the different sites within the Lucky Strike vent field that occur at different water depth within the field (Table 1) over the PC1 and PC2 space contrast with the interpretation of Bogdanov et al. (2006), who suggested that, due to phase separation occurring at the seafloor or in the shallow subseafloor, the highest temperature fluids occur at the deepest vents within the vent field. This phase separation was hypothesized to be a main control on the variability of composition of the hydrothermal deposits (Bogdanov et al., 2006). However, our data indicates no systematic variation in bulk geochemistry with water depth or deposit age (~6,600 years to present; Sánchez-Mora et al., submitted). Therefore, differences in mineral assemblages and geochemistry likely only reflects the stage (low- or high- temperature) at which the sample was formed and not necessarily linked to phase separation.

5.1. Controls on minor and trace element distributions at Lucky Strike

Minor and trace elements occur within the main mineral phases (chalcopyrite, marcasite, pyrite and sphalerite) in hydrothermal sulfide deposits and can be incorporated into their crystal structure or can occur as micro- or nano-scale inclusions (Cook et al., 2016; Fontboté et al., 2017; Monecke et al., 2016). Minor and trace element distribution is generally evaluated via microanalytical techniques such as an electron microprobe and/or laser ablation ICP-MS (e.g., Berkenbosch et al., 2019; Grant et al., 2018; Keith et al., 2016; Melekestseva et al., 2017). Our approach uses PCA on bulk geochemistry of hydrothermal samples from the Lucky Strike vent field to determine the minor and trace element variability, which we compared to previous geochemical work conducted at Lucky Strike by Bogdanov et al. (2006) and compared to other similar studies on mid-ocean ridges.

The mineralogy of the Lucky Strike hydrothermal deposits are typical for basalt hosted mid-ocean ridge deposits, which is generally dominated by marcasite, pyrite, sphalerite, and chalcopyrite with the notable exception of the high abundance of barite, which has been linked to high Ba concentrations in the underlying E-MORB substrate (Langmuir et al., 1992). High-temperature interiors of chimneys are dominated by chalcopyrite and euhedral pyrite and marcasite. Concentrations of In, Se, Co and Sn correlate with the major mineral-forming elements (Cu, Fe, and S) that comprise this high-temperature mineral assemblage (Figure 5). These associations have been documented in other seafloor hydrothermal sites (e.g., Auclair et al., 1987; Hannington et al., 1991). Cobalt has been previously documented to be concentrated in marcasite and pyrite at Lucky Strike (Bogdanov et al., 2006). The correlation between Co with Cu and Fe that are associated with the precipitation of minerals at high-temperatures suggests that Co is hosted in euhedral pyrite and marcasite that precipitated associated with these high-temperature mineral assemblages

(Figure 5). At the basalt-hosted TAG hydrothermal field further south on the MAR, In is hosted primarily as a trace metal within chalcopyrite and marcasite, Sn is largely hosted within chalcopyrite, and Se is largely hosted in chalcopyrite and pyrite to a lesser extent (Grant et al., 2018). Similarly, Lein et al. (2010) and Bogdanov et al. (2008) report high concentrations of In within high-temperature mineral assemblages at Menez Gwen and Broken Spur, respectively, both also located at the MAR to the North and South of Lucky Strike, respectively. Selenium has also been documented to occur primarily within chalcopyrite at Lucky Strike (Rouxel et al., 2004) but also in pyrite in a range of other seafloor hydrothermal deposits (e.g., Monecke et al., 2016, and references therein).

The lower temperature exteriors of chimneys from Lucky Strike are dominated by sphalerite (ZnS), barite ($BaSO_4$), plumose marcasite and amorphous silica. Silver, Au, As, Ga, Cd, Sb, Tl, Pb, and Ge abundances correlate with the major mineral-forming elements (Zn, Ba, and Si) of this lower temperature mineral suite. The association of some of these trace elements (As, Sb, Cd, Mn, and Ag) with lower temperature minerals in the PCA (Figure 5) such as marcasite and sphalerite has been documented at Lucky Strike (Bogdanov et al., 2006) as well as at other hydrothermal deposits hosted on the MAR, including Menez Gwen (Lein et al., 2010), TAG (Grant et al., 2018), Broken Spur (Bogdanov et al., 2008).

The elements Ca, Ba, and Sr, which are associated with the sulfate minerals anhydrite and barite, have a distinct negative loading with respect to PC2. Barium and Sr have minor positive loadings and Ca has a minor negative loading with respect to PC1 (Figure 5). The minor negative loading of Ca with respect to PC1 is consistent with anhydrite occurring primarily in association with the high-temperature sulfide mineral suite due to its absence at lower temperatures due to its retrograde solubility at temperatures below 150°C (Blount & Dickson, 1969). In contrast, Ba and Sr have a positive loading with respect to PC1, consistent with the typical association of barite with lower-temperature sulfide minerals (Jamieson et al., 2016). The proximity of Sr to Ba in Figure 5 is likely the result of barite being significantly more abundant than anhydrite at Lucky Strike, as indicated by the higher Ba concentrations (and higher barite contents) in the samples compared to Ca.

Magnesium, V, Ni, and to a lesser extent, Mo and Na have a negative loading with respect to PC1 (Figure 5). At TAG, redox-sensitive elements such as V, Ni, and Mo are associated with the precipitation of pyrite and marcasite that has interacted with cold, Na- and Mg-rich seawater towards the exteriors of vents (Grant et al., 2018). Alternatively, Ni, and V can also be associated with the formation and scavenging of Fe-oxyhydroxides (German & Seyfried, 2014). Regardless, the negative loading with respect to PC2 discriminates elements associated with sulfate and oxide minerals that precipitate upon direct interactions with seawater, which is consistent with the three samples with the lowest PC2 loadings that are barite and Fe-oxyhydroxides rich.

5.2. Differences in S isotope compositions between the main Lucky Strike field and Capelinhos

Overall, the sulfur isotope compositions of the sulfide deposits at Lucky Strike range between -2.5 and 8.7‰ (Figure 7), which is within the range of average $\delta^{34}S$ values for sulfide minerals at other sediment-free and basalt-hosted mid-ocean ridge hydrothermal deposits (Hannington et al., 2005; Zeng et al., 2017). The range in $\delta^{34}S$ values for the main field reported in this study are similar to those reported by Rouxel et al. (2004). The mineralogy of the Capelinhos site is similar to the mineralogy of the deposits at the main field, which is consistent with evidence from vent fluid

trace element concentrations that correlate with chlorinity and indicate a common hydrothermal fluid source for these sites (Chavagnac et al., 2018). However, the S isotope compositions of sulfide minerals from Capelinhos are ~3.5‰ higher than the average values at the main field (Figure 7). The range at Capelinhos is comparable to other sediment-free fast to slow spreading mid-ocean ridges sites such as TAG, East Pacific Rise South, and Axial Seamount (Hannington et al., 2005; Zeng et al., 2017).

At mid-ocean ridge-hosted hydrothermal sites, $\delta^{34}S$ values of between ~0 and 10‰ are usually interpreted to be a result of two component mixing between igneous-derived sulfur ($\delta^{34}S \approx 0$‰) leached from mid-ocean ridge crust and seawater sulfate ($\delta^{34}S = 21$‰); (Hannington et al., 2005; Shanks, 2001; Zeng et al., 2017). It is possible that the more positive $\delta^{34}S$ values for sulfide minerals at Capelinhos are due to a higher relative contribution of reduced sulfur derived from seawater sulfate or a longer fluid flow pathway feeding the Capelinhos vents, or a combination of both (Chavagnac et al., 2018; Escartín et al., 2015). Also, in sediment free environments, the addition of isotopically-light H_2S associated with disproportionation of magmatic SO_2 can also drive the overall system towards lower $\delta^{34}S$ values (Gamo et al., 1997; McDermott et al., 2015; Shanks, 2001). Fluctuations in vent fluid CO_2 content (Pester et al., 2012) and recent magmatic intrusions detected from seismicity at Lucky Strike (Dziak et al., 2004) indicate that magmatic volatiles may contribute to the hydrothermal system. A higher proportion of such volatiles could result in the relatively lower $\delta^{34}S$ values in the hydrothermal precipitates in the main field. However, CO_2 fluid data is not available for Capelinhos to assess differences in volatile input between this site and the main field. In addition, there is no mineralogical evidence of direct magmatic volatile input, such as the presence of high-sulfidation alteration assemblages, sulfosalts, and elevated concentrations of volatile associated trace elements such as Bi, Se, and Te (Martin et al., 2019; de Ronde et al., 2011). Rouxel et al. (2004) speculate that, at Lucky Strike, there is also a component of a fractionated sulfur source associated with microbial activity below the fossil lava lake. These interpretations highlight the ambiguity inherent in the interpretation of $\delta^{34}S$ values on their own and the requirement of additional information to assess processes driving different sulfur isotope compositions at Lucky Strike.

Vent fluids at the main field are also depleted in Fe, enriched in Cl, and contain higher $^{87}Sr/^{86}Sr$, relative to Capelinhos fluids (Chavagnac et al., 2018). Chavagnac et al. (2018) interpret the higher $^{87}Sr/^{86}Sr$ at the main field to indicate higher rock/water ratios, even though the field lies directly above the heat source and the overall flow pathway is likely shorter. Longer residence times for fluids venting at the main field may result from locally reduced permeability. The fossil lava lake may act as a hydrological cap for ascending fluids, promoting lower overall permeabilities in the subsurface (Arnulf et al., 2014) leading to increased interaction with altered basalts, thus driving the $\delta^{34}S$ values of the fluids and deposits closer to zero (Figure 8).

Chavagnac et al. (2018) report a ~65% depletion in the dissolved Fe concentration of the fluids from the main field, relative to Capelinhos. Concentrations of other dissolved species (e.g., Mg, Mn, Na, and SO_4) and vent fluid pH indicate that this depletion is not a result of seawater dilution. Therefore it is suggested that significant amounts of precipitation of Fe-bearing minerals occur in the subseafloor below the main field (Chavagnac et al., 2018). The precipitation of pyrite/marcasite would result in a temperature-dependent S isotope fractionation between the precipitated pyrite/marcasite and reduced S in the fluid. The fraction of reduced S removed from the fluid due

to subseafloor pyrite/marcasite precipitation can be modelled over a range of temperatures as an open system Rayleigh distillation:

$$R = R_0 f^{(\alpha-1)}$$

where R is the isotopic ratio of the fraction f of reduced sulfur remaining in the fluid after pyrite/marcasite precipitation, R_0 is the initial sulfur isotope ratio of the fluid, and α is the fractionation factor ($\alpha = R_{Py}/R_{H2S}$). Compared to the vent fluids at the main field, the composition of the endmember venting fluids at Capelinhos have been interpreted to be more representative of the fluids within the deeper part of the hydrothermal reaction zone, based on the linear correlation of trace elements and chlorinity in the hydrothermal fluids at Lucky Strike (Chavagnac et al., 2018; Pester et al., 2012). The $\delta^{34}S$ values from sulfide minerals at Capelinhos can therefore be used to represent R_0 (i.e., the isotopic composition of the ascending fluids below the main field) and the $\delta^{34}S$ values from the main field represent R. The temperature dependent fractionation factors (α), determine the different mass fractions (f) at which the ~3.5‰ difference between Capelinhos and main Lucky Strike can be obtained. If fractionation factors are used between H_2S and pyrite (Ohmoto & Rye, 1979) from 150 and 350°C , fractions of 0.21 to 0.034 are obtained, respectively (Hannington, 2014).

Results from sulfur isotope modelling suggest that at least ~80% of the original H_2S in the hydrothermal fluid at the main field precipitated below the seafloor, dominantly as pyrite/marcasite (Figure 8). A similar proportion (75%) of major and trace element deposition below the seafloor has been estimated at the seawater-dominated Reykjanes geothermal system in Iceland, which is considered an analogue to seafloor systems (Grant et al., 2020). The average value of H_2S in hydrothermal fluids at the main field vents is 2.7 mmol/kg (Charlou et al., 2000). If this value represents less than 20% of the original H_2S concentration, the original fluid H_2S concentration would have been greater than ~14 mmol/kg. The amount of reduced S trapped in the subsurface as pyrite/marcasite is reasonably consistent with the amount of Fe estimated to have been trapped in the subsurface based on differences in vent fluid chemistry between the main field and Capelinhos (Chavagnac et al., 2018).

Chalcopyrite is another Fe-bearing mineral that could have precipitated and trapped both Fe and S in the subsurface and commonly forms in the upflow zones of seafloor hydrothermal systems (Franklin et al., 2005; Galley et al., 2007). However, the fractionation factors between chalcopyrite and H_2S at subseafloor hydrothermal conditions are extremely low (e.g., <0.3 (1000lnα) at 150°C, Ohmoto and Rye, 1979) and very large amounts of reduced sulfur would have to precipitate in the subsurface to generate the predicted fractionations, requiring initial fluid H_2S concentrations of >300,000 mmol. For comparison, maximum reported H_2S concentrations for vent fluids are on the order of 110 mmol (Von Damm et al., 1995). Therefore, although chalcopyrite may be precipitating in the subseafloor, the isotopic differences between Capelinhos and the main field suggest that pyrite is the primary sulfide phase being precipitated. This interpretation is consistent with evidence from subsea drilling at TAG and from VMS deposits that show that upflow zones can be enriched in chalcopyrite but are dominated by pyrite (Galley et al., 2007; Knott et al., 1998).

It should be noted that the calculations and results presented above are predicated assuming isotopic equilibrium between the vent fluid and minerals. In seafloor hydrothermal systems, isotopic equilibrium can be evaluated comparing known temperatures of formation to temperatures calculated between mineral pairs-based equilibrium sulfur isotope fractionation. For example,

there is a uniform difference in isotopic composition of ~3‰ between neighboring chalcopyrite and marcasite crystals at both the main field and Capelinhos (Figures 6). This difference is independent of sample location, and depositional age as there is no significant variation in $\delta^{34}S$ values and mineral textures (e.g., plumose vs. euhedral marcasite) (Sánchez-Mora et al. submitted). The isotopic enrichment in ^{34}S in chalcopyrite, relative to marcasite, is consistent with equilibrium fractionation processes. Under equilibrium conditions, a 3‰ fractionation between chalcopyrite and marcasite corresponds to a crystallization temperature of 114°C (using fractionation factors by Kajiwara and Krouse, 1971). This temperature is likely too low for typical crystallization temperatures for chalcopyrite (>250˚C) although marcasite can form at temperatures of up to 240˚C under hydrothermal conditions (Hannington et al., 1995; Murowchick & Barnes, 1986), suggesting that these mineral phases were not in isotopic equilibrium at the time of formation. This is consistent with textural evidence that indicates that these mineral phases did not co-precipitate (Figure 6), and the difference in isotopic composition between the two mineral phases is likely a result of either equilibrium or non-equilibrium isotopic partitioning between each mineral phase and the hydrothermal fluid at different temperatures of mineral formation and/or other possible kinetic isotopic effects, such as effects of microbial processes during marcasite formation (Juniper et al., 1988). Overall, an important outcome from this analysis is that subsurface sulfide mineral precipitation can change the S isotopic composition of the vent fluid and surficial deposits (Figure 8), yielding surficial isotopic compositions that are indistinguishable from isotopic compositions that result from simple two-component mixing between mantle sulfur and reduced seawater sulfate (Ohmoto & Lasaga, 1982; Ono et al., 2007).

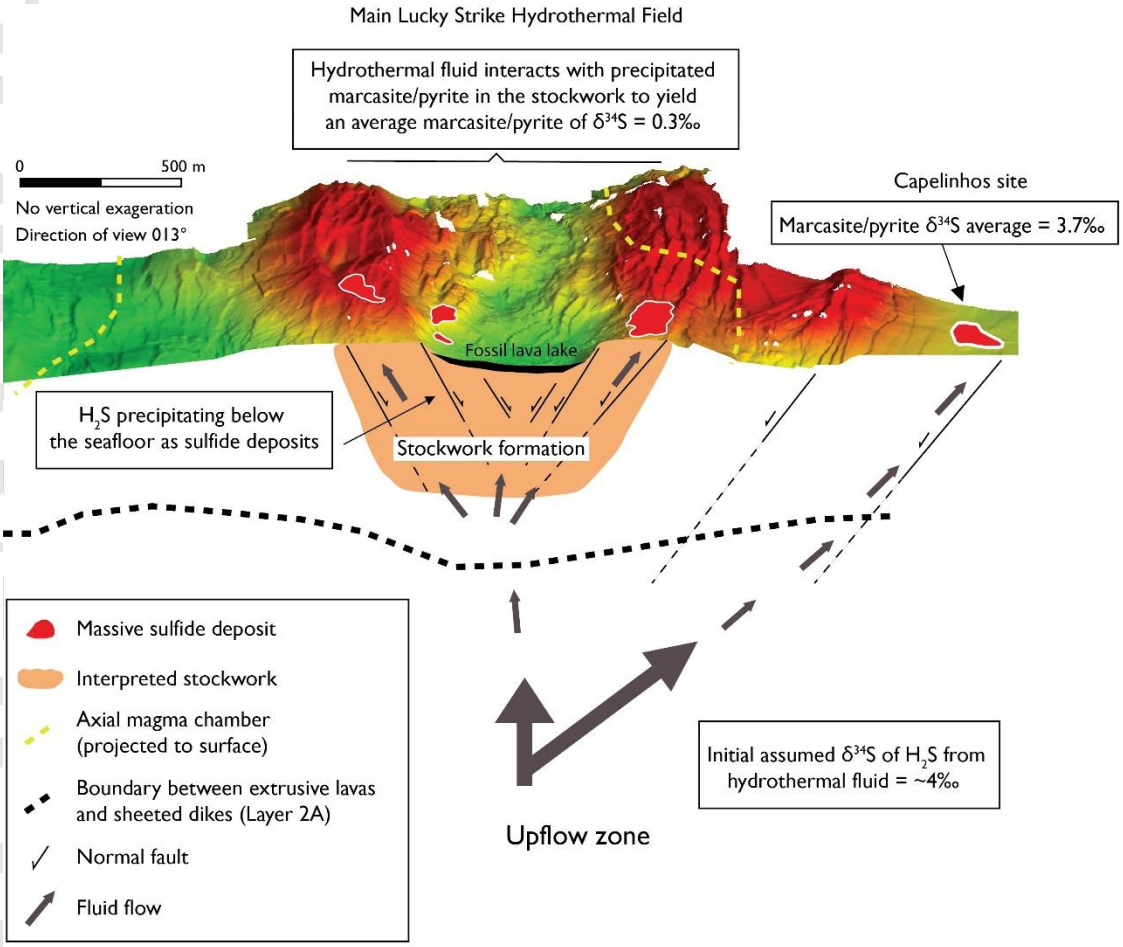

Figure 8. Summary sketch of the location and faulting at the Lucky Strike hydrothermal field. The stockwork is interpreted based on the sulfur isotope data from this study. Axial magma chamber (~3.5 km depth) outline from Combier et al. (2015) and layer 2A from Seher et al. (2010), both derived from seismic reflection data.

5.3. Geological controls on the composition of Lucky Strike and other vent fields along the Mid-Atlantic Ridge

The most distinctive compositional characteristic of both Lucky Strike and Menez Gwen (a vent field located ~90 km northeast from Lucky Strike, closer to the Azores hotspot) is the abundance of barite (Bogdanov et al., 2005; Lein et al., 2010). Compared to other basalt or ultramafic-hosted vent fields along the MAR that are not hotspot influenced, such as TAG, Snake Pit, and Rainbow, Lucky Strike contains significantly more barite, and higher concentrations of Ba, Sr and Mo, but lower Au and Sn (Figure 9);(Bogdanov et al., 2002; Fouquet et al., 1993; Grant et al., 2018;

Honnorez et al., 1990; Krasnov et al., 1995; Marques et al., 2007). The basaltic substrate at Lucky Strike and Menez Gwen is dominated by E-MORB (Gale et al., 2011; Langmuir et al., 1997), which is enriched in incompatible elements (e.g., Ba and Sr) compared to the normal mid-ocean ridge basalts (N-MORB) that host TAG and Snake Pit (Hannington et al., 2005). The E-MORB substrate composition and associated enrichment in incompatible elements (Ba and Sr) is linked to the melting of the metasomatized mantle associated with the Azores hotspot (Langmuir et al., 1997).

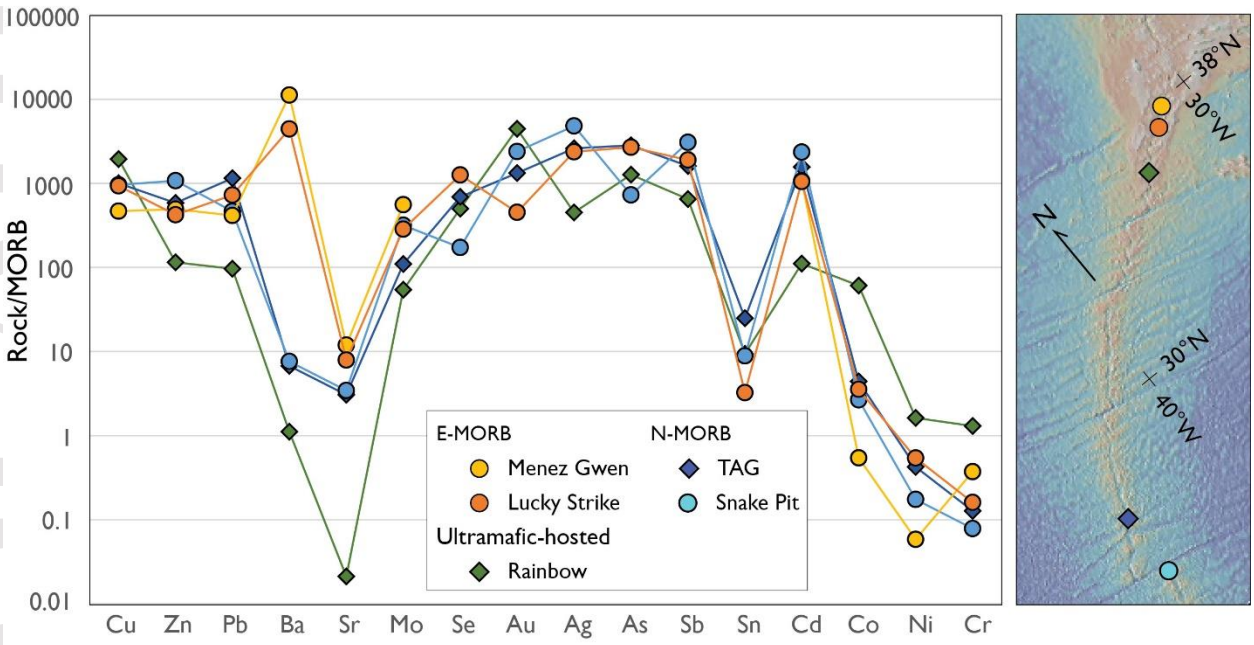

Figure 9. Average bulk geochemistry of hydrothermal samples of selected Mid-Atlantic Ridge hosted hydrothermal sites, normalized to average mid-ocean ridge basalt composition (Arevalo & McDonough, 2010). The diamond symbol indicates sites hosted in detachment fault systems. Lucky Strike data is from this study and Bogdanov et al. (2006), Menez Gwen (Bogdanov et al., 2005), TAG (Hannington et al., 1991; Hannington, 1993; Krasnov et al., 1995; Lisitsyn et al., 1990; Rona et al., 1993; Thompson et al., 1988), Snake Pit (Hannington et al., 1991; Honnorez et al., 1990; Kase et al., 1990; Krasnov et al., 1995; Fouquet et al., 1993), and Rainbow (Bogdanov et al., 2002; Marques et al., 2007). Menez Gwen (n=12), Lucky Strike (n=50), Rainbow (n=6), TAG (n=190), and Snake Pit (n=105). Full dataset provided in supporting information Table S2.

In contrast to E-MORB hosted Lucky Strike and Menez Gwen, the active TAG mound, which contains relatively low concentrations of Ba and Sr, is hosted within N-MORB in an active detachment fault zone (Humphris et al., 2015). Rainbow is hosted in ultramafic rocks but is influenced by basaltic rocks in the vicinity of the hydrothermal site. Rainbow has a relatively high Ni and Co content, which is typical for ultramafic-hosted sites (Marques et al., 2007; Mozgova et al., 2008). At ultramafic sites, serpentinization causes the release of Co and Ni during the alteration of primary silicate minerals such as olivine (Marques et al., 2007). Barium enrichment in E-MORB hosted hydrothermal sites and Co enrichment in ultramafic hosted hydrothermal sites have been widely documented (e.g., Hannington et al., 2005). The Ba/Co ratio within hydrothermal deposits

can therefore be used to discriminate E-MORB hosted deposits from deposits hosted on other mafic and ultramafic substrates at sites where the composition of the host rock is not known (Figure 10a). To test the utility of this ratio, a compilation of four groups of substrate types were compiled (Table S2) for which bulk geochemistry of hydrothermal deposits was available: 1) E-MORB (Lucky Strike, Menez Gwen, and Endeavour); 2) N-MORB (TAG, Snake Pit, and Broken Spur); 3) ultramafic (Rainbow and Logatchev); and 4) mixed mafic and ultramafic (Beebe, Kairei, Yuhuang-1, and Daxi; Figure 10a, b). The median Ba/Co values are 180, 3, 3, and 0.006 for E-MORB, N-MORB, ultramafic, and mixed mafic/ultramafic groups, respectively (Figure 10b). However, concentrations of Ba and Co can also be significantly affected by temperature during mineral precipitation, with Co associated with high-temperature mineral assemblages and Ba associated with lower-temperature mineral assemblages (Figure 5). Therefore, to test whether changes in Ba/Co values primarily reflect substrate composition or temperature, the ratios are plotted against Cu/Zn, another geochemical proxy for temperature, for the different substrate groups (Figure 10). Elevated Cu values are associated with precipitation of high-temperature chalcopyrite (250-350°C) and high Zn values are associated with precipitation of sphalerite at lower temperatures (<250°C; Figure 5; Hannington, 2014). For the E-MORB group, the Ba/Co values show a general negative trend, relative to Cu/Zn, which reflects the temperature dependence of both ratios within a group. However, when comparing data from different substrate groups, the Ba/Co shows a trend associated with different substrates that is independent of Cu/Zn (Figure 10).

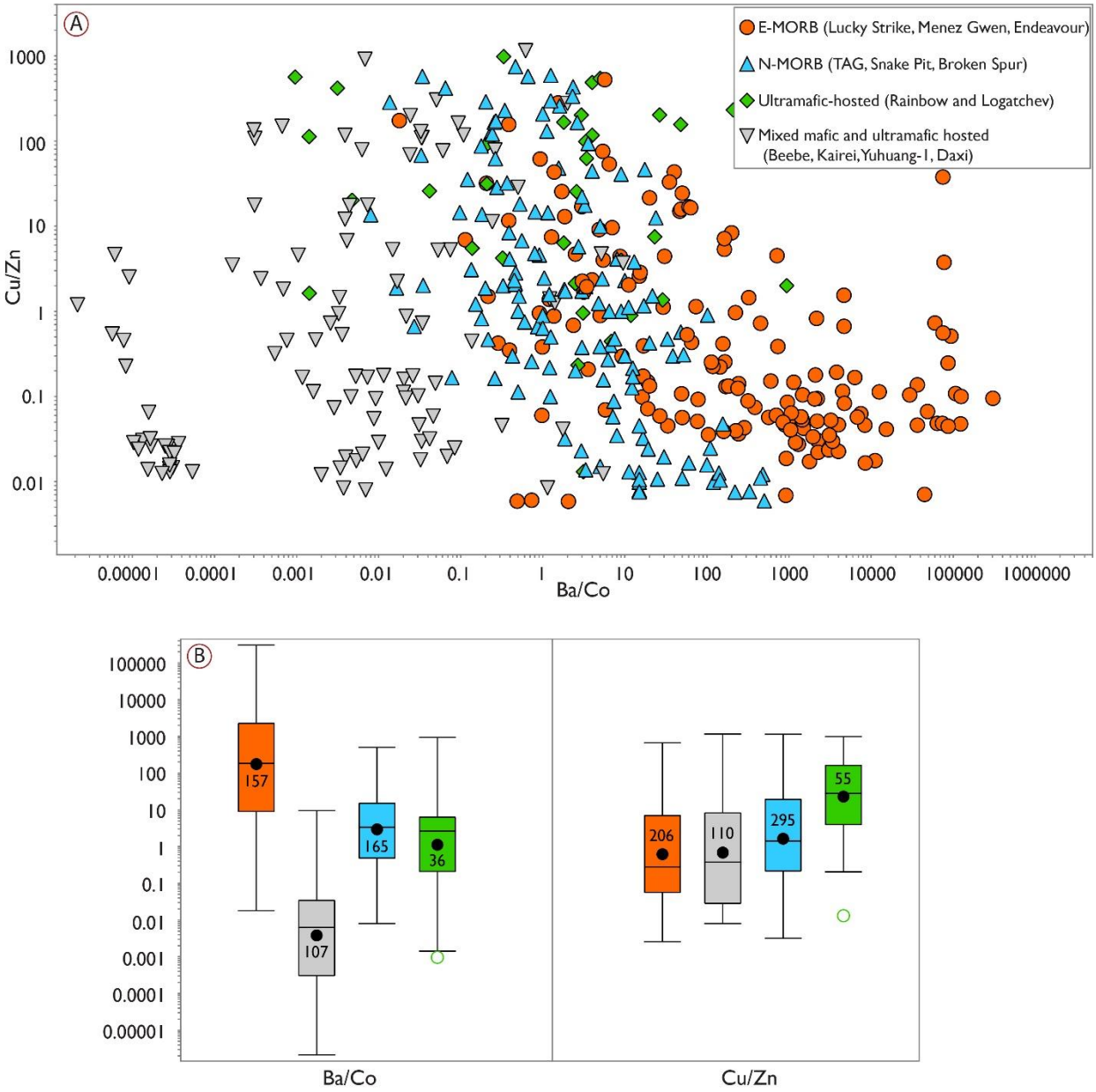

Figure 10. A) Ratios from selected SMS deposits grouped according to host rock in mid-ocean ridges. Ba/Co vs Cu/Zn. Ba/Co ratio used as a proxy for proximity to a hotspot, Cu/Zn used as a proxy of temperature of formation. B) Box and whisker plots of quartiles for Ba/Co and Cu/Zn (boxes with black line for median, black dot for mean, and number of samples). E-MORB includes data from Lucky Strike (this study and Bogdanov et al. (2006)), Menez Gwen (Bogdanov et al., 2005), and Endeavour (Morgan & Selk, 1984; Samson, 1986; Margaret K. Tivey & Delaney, 1986; Margaret Kingston Tivey et al., 1999; Toffolo et al., 2020). N-MORB includes TAG (Hannington et al., 1991; Hannington, 1993; Krasnov et al., 1995; Lisitsyn et al., 1990; Rona et al., 1993; Thompson et al., 1988), Snake Pit (Hannington et al., 1991; Honnorez et al., 1990; Kase et al., 1990; Krasnov et al., 1995; Fouquet et al., 1993; Toffolo et al., 2020), and Broken Spur (Bogdanov et al., 1995; Bogdanov et al., 2008; Lisitsyn et al., 1999; Peresypkin et al., 1999; Toffolo et al., 2020). Ultramafic-hosted includes Rainbow (Marques et al., 2007) and Logatchev (Bogdanov et

al., 1997; Krasnov et al., 1995; Lisitsyn et al., 1999; Mozgova et al., 1999; Murphy & Meyer, 1998; Peresypkin et al., 1999). Mixed mafic and ultramafic includes Beebe (Webber et al., 2015), Kairei (Wang et al., 2014), Yuhuang-1 (Liao et al., 2018), and Daxi (Wang et al., 2021). Data in Table S2.

6. Conclusions

The hydrothermal deposits at Lucky Strike are composed of a mineral assemblage typical of basalt-hosted mid-ocean ridge hydrothermal deposits, except for the presence of abundant barite. Principal component analysis discriminates the minor and trace element distribution between high and low temperature mineral assemblages and the precipitation of minerals that result from direct interaction with seawater. The mineralogy and geochemical composition of the off-axis Capelinhos site is similar to the deposits from the main field. However, the sulfur isotopic composition of Capelinhos is heavier by ~3.5‰ compared to the rest of Lucky Strike. These differences reflect variations in length and/or permeability in the pathways of the uprising hydrothermal fluid and distinct fluid/rock interactions at each of these sites, including evidence from S isotope modelling of extensive subseafloor marcasite/pyrite mineralization below the main site. Here, S isotopic data corroborate previously reported variations in fluid chemistry between different sites that indicate that >80% of the available H_2S in the ascending hydrothermal fluid precipitates in a stockwork zone below the seafloor. These results highlight that the interpretation of S isotope compositions for hydrothermal deposits along mid-ocean ridges cannot necessarily be interpreted simply within the context of a two-component mixing model between mantle- and seawater-derived sulfur sources, and that subseafloor mineralization and isotopic exchange can also affect the isotopic compositions of surficial sulfide deposits.

The Ba/Co ratio of hydrothermal deposits provides a temperature-independent geochemical tool to discriminate the composition of the substrate beneath hydrothermal vent fields at mid-ocean ridges, especially E-MORB hosted site that have a distinct elevated Ba/Co ratio. High Ba/Co ratios at Lucky Strike and Menez Gwen indicate an E-MORB substrate associated with the Azores hotspot. In contrast, low Ba/Co ratios, are associated with hydrothermal sites hosted in N-MORB, ultramafic, and sites that have a mixed mafic and ultramafic substrates.

Acknowledgments

This work was supported by the Canada Research Chair Program, an NSERC Discovery Grant, and RDC Leverage Grant to J.W. Jamieson. DSM acknowledges support from the NSERC iMAGE-CREATE program.

Data availability statement

All the geochemical data (bulk geochemistry and *in situ* sulfur isotope) is included in this paper and in the Supporting Information and can be also accessed at https://doi.org/10.5281/zenodo.6035032 (Sánchez-Mora et al., 2022).

References

Arevalo, R. J., & McDonough, W. F. (2010). Chemical variations and regional diversity observed in MORB. *Chemical Geology*, *271*, 70–85.

Argus, D. F., Gordon, R. G., & Demets, C. (2011). Geologically current motion of 56 plates relative to the no-net-rotation reference frame. *Geochemistry, Geophysics, Geosystems*, *12*(11), 1–13. https://doi.org/10.1029/2011GC003751

Arnulf, A. F., Harding, A. J., Kent, G. M., Singh, S. C., & Crawford, W. C. (2014). Constraints on the shallow velocity structure of the Lucky Strike Volcano, Mid-Atlantic Ridge, from downward continued multichannel streamer data. *Journal of Geophysical Research, Solid Earth*, *119*, 1119–1144. https://doi.org/10.1002/2013JB010500

Auclair, G., Fouquet, Y., & Bohn, M. (1987). Distribution of selenium in high-temperature hydrothermal sulfide deposits at 13° North, East Pacific Rise. *The Canadian Mineralogist*, *25*, 577–587.

Barreyre, T., Escartín, J., Sohn, R. A., Cannat, M., Ballu, V., & Crawford, W. C. (2014). Temporal variability and tidal modulation of hydrothermal exit-fluid temperatures at the Lucky Strike deep-sea vent field, Mid-Atlantic Ridge. *Journal of Geophysical Research: Solid Earth*, *119*, 2543–2566. https://doi.org/10.1002/2013JB010478

Barreyre, T., Escartín, J., Garcia, R., Cannat, M., Mittelstaedt, E., & Prados, R. (2012). Structure, temporal evolution, and heat flux estimates from the Lucky Strike deep-sea hydrothermal field derived from seafloor image mosaics. *Geochemistry, Geophysics, Geosystems*, *13*(4), 1–29. https://doi.org/10.1029/2011GC003990

Berkenbosch, H. A., de Ronde, C. E. J., Ryan, C. G., McNeill, A. W., Howard, D. L., Gemmell, J. B., & Danyushevsky, L. V. (2019). Trace element mapping of copper- and zinc-rich black smoker chimneys from brothers volcano, kermadec arc, using synchrotron radiation XFM and LA-ICP-MS. *Economic Geology*, *114*(1), 67–92. https://doi.org/10.5382/econgeo.2019.4620

Blandin, J., Sarradin, P. M., & Cannat, M. (2013). MOMARSAT2013 cruise, RV Pourquoi pas ? https://doi.org/10.17600/13030040

Blount, C. W., & Dickson, F. W. (1969). The solubility of anhydrite (CaSO4) in NaCl-H2O from 100 to 450°C and 1 to 1000 bars. *Geochimica et Cosmochimica Acta*, *33*, 227–245. https://doi.org/10.1016/0016-7037(69)90140-9

Bogdanov, Y. A., Gurich, E., & Kuptsov, V. (1995). Relict sulfide mounds at the TAG hydrothermal field of the Mid-Atlantic Ridge (26° N, 45° W). *Oceanology*, *34*, 534–542.

Bogdanov, Y. A., Bortnikov, N. S., Sagalevich, A. M., Gurvich, E. G., & Vikent'ev, I. V. (1997). New type of mineral-forming systems: Black smokers of the hydrothermal field at 14° 45'

N MAR. *Geologiya Rudnykh (Geology of Ore Deposits)*, *39*, 68–90.

Bogdanov, Y. A., Bortnikov, N. S., Vikent'ev, I. V., Lein, A. Y., Gurvich, E. G., Sagalevich, A. M., et al. (2002). Mineralogical-Geochemical Peculiarities of Hydrothermal Sulfide Ores and Fluids in the Rainbow Field Associated with Serpentinites, Mid-Atlantic Ridge (36°14'). *Geology of Ore Deposits*, *44*(6), 444–473.

Bogdanov, Y. A., Lein, A. Y., & Sagalevich, A. M. (2005). Chemical Composition of the Hydrothermal Deposits of the Menez Gwen Vent Field (Mid-Atlantic Ridge). *Marine Geology*, *45*(6), 849–856.

Bogdanov, Y. A., Lein, A. Y., Sagalevich, A. M., Ul'yanov, A. A., Dorofeev, S. A., & Ul'yanova, N. V. (2006). Hydrothermal sulfide deposits of the Lucky Strike vent field, Mid-Atlantic Ridge. *Geochemistry International*, *44*(4), 403–418. https://doi.org/10.1134/S0016702906040070

Bogdanov, Y. A., Lein, A. Y., Maslennikov, V. V., Li, S., & Ul'yanov, A. A. (2008). Mineralogical – Geochemical Features of Sulfide Ores from the Broken Spur Hydrothermal Vent Field. *Oceanology*, *48*, 679–700. https://doi.org/10.1134/S000143700805007X

Cannat, M., & Sarradin, P. M. (2012). MOMARSAT2012 cruise, RV Thalassa. https://doi.org/10.17600/12040050

Cannat, M., Briais, A., Deplus, C., Escartín, J., Georgen, J., Lin, J., et al. (1999). Mid-Atlantic Ridge-Azores hotspot interactions: Along-axis migration of a hotspot-derived event of enhanced magmatism 10 to 4 Ma ago. *Earth and Planetary Science Letters*, *173*(3), 257–269. https://doi.org/10.1016/S0012-821X(99)00234-4

Cannat, M., Blandin, J., & Sarradin, P. M. (2011). MOMARSAT2011 cruise, RV Pourquoi pas ? https://doi.org/10.17600/11030070

Charlou, J. L., Donval, J. P., Douville, E., Jean-Baptiste, P., Radford-Knoery, J., Fouquet, Y., et al. (2000). Compared geochemical signatures and the evolution of Menez Gwen (35°50N) and Lucky Strike (37°17N) hydrothermal fluids, south of the Azores Triple Junction on the Mid-Atlantic Ridge. *Chemical Geology*, *171*(1–2), 49–75. https://doi.org/10.1016/S0009-2541(00)00244-8

Chavagnac, V., Leleu, T., Fontaine, F., Cannat, M., Ceuleneer, G., & Castillo, A. (2018). Spatial Variations in Vent Chemistry at the Lucky Strike Hydrothermal Field, Mid-Atlantic Ridge (37°N): Updates for Subseafloor Flow Geometry From the Newly Discovered Capelinhos Vent. *Geochemistry, Geophysics, Geosystems*, *19*(11), 4444–4458. https://doi.org/10.1029/2018GC007765

Combier, V., Seher, T., Singh, S. C., Crawford, W. C., Cannat, M., Escartín, J., & Dusunur, D. (2015). Three-dimensional geometry of axial magma chamber roof and faults at Lucky Strike volcano on the Mid-Atlantic Ridge. *Journal of Geophysical Research : Solid Earth*, *121*, 6386–6403. https://doi.org/10.1002/2015JB012282.Received

Cook, N., Ciobanu, C. L., George, L., Zhu, Z. Y., Wade, B., & Ehrig, K. (2016). Trace element

analysis of minerals in magmatic-hydrothermal ores by laser ablation inductively-coupled plasma mass spectrometry: Approaches and opportunities. *Minerals*, *6*(4). https://doi.org/10.3390/min6040111

Crawford, W. C., Rai, A., Singh, S. C., Cannat, M., Escartín, J., Wang, H., et al. (2013). Hydrothermal seismicity beneath the summit of Lucky Strike volcano, Mid-Atlantic Ridge. *Earth and Planetary Science Letters*, *373*, 118–128. https://doi.org/10.1016/j.epsl.2013.04.028

Von Damm, K. L., Oosting, S. E., Kozlowski, R., Buttermore, L. G., Colodner, D. C., Edmonds, H. N., et al. (1995). Evolution of East Pacific Rise hydrothermal vent fluids following a volcanic eruption. *Nature*, *375*(6526), 47–50. https://doi.org/10.1038/375047a0

Von Damm, K. L., Bray, A. M., Buttermore, L. G., & Oosting, S. E. (1998). The geochemical controls on vent fluids from the Lucky Strike vent field , Mid-Atlantic Ridge. *Earth and Planetary Science Letters*, *160*, 521–536.

Ding, T., Valkiers, S., Kipphardt, H., De Bièvre, P., Taylor, P. D. P., Gonfiantini, R., & Krouse, R. (2001). Calibrated sulfur isotope abundance ratios of three IAEA sulfur isotope reference materials and V-CDT with a reassessment of the atomic weight of sulfur. *Geochimica et Cosmochimica Acta*, *65*(15), 2433–2437.

Doe, B. R. (1994). Zinc, Copper, and Lead in Midocean Ridge Basalts and the Source-Rock Control on Zn/Pb in Ocean-Ridge Hydrothermal Deposits. *Geochimica Et Cosmochimica Acta*, *58*(10), 2215–2223.

Dziak, R. P., Smith, D. K., Bohnenstiehl, D. W. R., Fox, C. G., Desbruyeres, D., Matsumoto, H., et al. (2004). Evidence of a recent magma dike intrusion at the slow spreading Lucky Strike segment, Mid-Atlantic Ridge. *Journal of Geophysical Research B: Solid Earth*, *109*(12), 1–15. https://doi.org/10.1029/2004JB003141

Eldridge, C. S., Barton, P. B., & Ohmoto, H. (1983). Mineral textures and their bearing on formation of the Kuroko orebodies. In H. Ohmoto & B. J. Skinner (Eds.), *The Kuroko and related volcanogenic massive sulfide deposits* (pp. 241–281). Economic Geology Monographs.

Escartín, J., Cannat, M., Pouliquen, G., Rabain, A., & Lin, J. (2001). Crustal thickness of V-shaped ridges south of the Azores: Interaction of the Mid-Atlantic Ridge (36°–39°N) and the Azores hot spot. *Journal of Geophysical Research*, *106*(B10), 21719–21735. https://doi.org/10.1029/2001JB000224

Escartín, J., Soule, S. A., Cannat, M., Fornari, D. J., Düşünür, D., & Garcia, R. (2014). Lucky Strike seamount: Implications for the emplacement and rifting of segment-centered volcanoes at slow spreading mid-ocean ridges. *Geochemistry, Geophysics, Geosystems*, *15*, 4157–4179. https://doi.org/10.1002/2014GC005563.Received

Escartín, J., Barreyre, T., Cannat, M., Garcia, R., Gracias, N., Deschamps, A., et al. (2015). Hydrothermal activity along the slow-spreading Lucky Strike ridge segment (Mid-Atlantic Ridge): Distribution, heatflux, and geological controls. *Earth and Planetary Science Letters*,

431, 173–185. https://doi.org/10.1016/j.epsl.2015.09.025

Fallon, E. K., Frische, M., Petersen, S., Brooker, R. A., & Scott, T. B. (2019). Geological, mineralogical and textural impacts on the distribution of environmentally toxic trace elements in seafloor massive sulfide occurrences. *Minerals*, *9*(3), 1–53. https://doi.org/10.3390/min9030162

Fontboté, L., Kouzmanov, K., Chiaradia, M., & Pokrovski, G. S. (2017). Sulfide minerals in hydrothermal deposits. *Elements*, *13*(2), 97–103. https://doi.org/10.2113/gselements.13.2.97

Fouquet, Y., Wafik, A., Cambon, P., Mevel, C., Meyer, G., & Gente, P. (1993). Tectonic Setting and Mineralogical and Geochemical Zonation in the Snake Pit Sulfide Deposit (Mid-Atlantic Ridge at 23°N). *Economic Geology*, *88*, 2018–2036.

Fouquet, Y., Charlou, J.-L., Costa, I., Donval, J.-P., Radford-Knoery, J., Pellé, H., et al. (1994). A detailed study of the Lucky Strike hydrothermal site and discovery of a new hydrothermal site: Menez Gwen. In *Preliminary results on the DIVA1 Cruise (5-29 May, 1994)* (pp. 14–17). InterRidge Newsletter.

Fouquet, Y., Cambon, P., Etoubleau, J., Charlou, J. L., Ondréas, H., Barriga, F. J. A. S., et al. (2010). Geodiversity of hydrothermal processes along the Mid-Atlantic ridge and ultramafic-hosted mineralization: A new type of oceanic Cu-Zn-Co-Au volcanogenic massive sulfide deposit. *Geophysical Monograph Series*, *188*, 321–367. https://doi.org/10.1029/2008GM000746

Franklin, J. M., Gibson, H. . L., Jonasson, I. R., & Galley, A. G. (2005). Volcanogenic Massive Sulfide Deposits. *Economic Geology 100th Anniversary Volume*, 523–560. https://doi.org/10.1016/B978-0-08-095975-7.01120-7

Gale, A., Escrig, S., Gier, E. J., Langmuir, C. H., & Goldstein, S. L. (2011). Enriched basalts at segment centers: The Lucky Strike (37°17'N) and Menez Gwen (37°50'N) segments of the Mid-Atlantic Ridge. *Geochemistry, Geophysics, Geosystems*, *12*(6). https://doi.org/10.1029/2010GC003446

Galley, A. G., Hannington, M. D., & Jonasson, I. R. (2007). Volcanogenic Massive Sulphide Deposits. *Mineral Deposits of Canada: A Synthesis of Major Deposit-Types, District Metallogeny, the Evolution of Geological Provinces, and Exploration Methods*, (5), 141–161.

Galley, A. G, Hannington, M. D., & Jonasson, I. R. (2007). Volcanogenic massive sulphide deposits. *Geological Association of Canada*, (5), 141–161.

Gamo, T., Okamura, K., Charlou, J., Urabe, T., Auzende, J., Ishibashi, J., et al. (1997). Acidic and sulfate-rich hydrothermal fluids from the Manus back-arc basin , Papua New Guinea. *Geology*, *25*, 139–142. https://doi.org/10.1130/0091-7613(1997)025<0139

Gente, P., Dyment, J., Maia, M., & Goslin, J. (2003). Interaction between the Mid-Atlantic Ridge and the Azores hot spot during the last 85 Myr: Emplacement and rifting of the hot spot-derived plateaus. *Geochemistry, Geophysics, Geosystems*, *4*(10), 1–23.

https://doi.org/10.1029/2003GC000527

German, C. R., & Seyfried, W. E. (2014). *Hydrothermal Processes*. *Treatise on Geochemistry* (2nd ed., Vol. 8). Elsevier Ltd. https://doi.org/10.1016/B978-0-08-095975-7.00607-0

Gini, C., Escartín, J., Cannat, M., & Barreyre, T. (2021). Extrusive upper crust formation at slow-spreading ridges: Fault steering of lava flows. *Earth and Planetary Science Letters*, *576*, 117202. https://doi.org/10.1016/j.epsl.2021.117202

Grant, H. L. J., Hannington, M. D., Petersen, S., Frische, M., & Fuchs, S. H. (2018). Constraints on the behavior of trace elements in the actively-forming TAG deposit, Mid-Atlantic Ridge, based on LA-ICP-MS analyses of pyrite. *Chemical Geology*, (July), 1–27. https://doi.org/10.1016/j.chemgeo.2018.08.019

Grant, H. L. J., Hannington, M. D., Hardardóttir, V., Fuchs, S. H., & Schumann, D. (2020). Trace metal distributions in sulfide scales of the seawater-dominated Reykjanes geothermal system: Constraints on sub-seafloor hydrothermal mineralizing processes and metal fluxes. *Ore Geology Reviews*, *116*(May 2019), 103145. https://doi.org/10.1016/j.oregeorev.2019.103145

Hannington, M. D., Herzig, P., Scott, S., Thompson, G., & Rona, P. (1991). Comparative mineralogy and geochemistry of gold-bearing sulfide deposits on the mid-ocean ridges. *Marine Geology*, *101*(1–4), 217–248. https://doi.org/10.1016/0025-3227(91)90073-D

Hannington, M. D., Jamieson, J., Monecke, T., Petersen, S., & Beaulieu, S. (2011). The abundance of seafloor massive sulfide deposits. *Geology*, *39*(12), 1155–1158. https://doi.org/10.1130/G32468.1

Hannington, M. D. (1993). The formation of atacamite during weathering of sulfides on the modern seafloor. *Canadian Mineralogist*, *31*(4), 945–956.

Hannington, M. D. (2014). Volcanogenic Massive Sulfide Deposits. *Treatise on Geochemistry: Second Edition*, *13*, 463–488. https://doi.org/10.1016/B978-0-08-095975-7.01120-7

Hannington, M. D., Jonasson, I. R., Herzig, P. M., & Petersen, S. (1995). Physical and chemical processes of seafloor mineralization at mid-ocean ridges. In Susan E. Humphris, R. A. Zierenberg, S. Mullineaux, & R. E. Thomson (Eds.), *Seafloor hydrothermal systems: Physical, chemical, biological, and geological interactions*, *Geophysical Monograph* (pp. 115–157). American Geophysical Union. https://doi.org/10.1029/GM091p0115

Hannington, M. D., Poulsen, K. H., Thompson, J. F. ., & Sillitoe, R. H. (1999). Volcanogenic gold in the massive sulfide environment. In C. T. Barrie & M. D. Hannington (Eds.), *Volcanic-associated massive sulfide deposits: Processes and examples in modern and ancient settings* (Vol. 8, pp. 319–350). Reviews in Economic Geology.

Hannington, M. D., de Ronde, C. E. J., & Petersen, S. (2005). Sea-Floor Tectonics and Submarine Hydrothermal Systems. *Economic Geology*, *100th Anni*, 111–141.

Haymon, R. M. (1983). Growth history of hydrothermal black smoker chimneys. *Nature*, *301*, 695–698.

Hoffman, E. L. (1992). Instrumental neutron activation in geoanalysis. *Journal of Geochemical Exploration*, *44*, 297–319.

Honnorez, C. M., Honnorez-Guerstein, B. M., & Tomschi, H. P. (1990). Mineralogy and chemistry of sulfide deposits drilled from hydrothermal mound of the Snake Pit active field, MAR. In R. Detrick, J. B. Honnorez, W. B. Bryan, & T. Juteau (Eds.), *Proceedings of the Ocean Drilling Program, Scientific Results* (Vol. 106/109, pp. 145–162). College Station.

Humphris, S. E., Fornari, D. J., Scheirer, D. S., German, C. R., & Parson, L. M. (2002). Geotectonic setting of hydrothermal activity on the summit of Lucky Strike Seamount (37°17'N, Mid-Atlantic Ridge). *Geochemistry, Geophysics, Geosystems*, *3*(8), 1–24. https://doi.org/10.1029/2001GC000284

Humphris, S. E., Tivey, M. K., & Tivey, M. A. (2015). The Trans-Atlantic Geotraverse hydrothermal field: A hydrothermal system on an active detachment fault. *Deep-Sea Research Part II: Topical Studies in Oceanography*, *121*, 8–16. https://doi.org/10.1016/j.dsr2.2015.02.015

Jamieson, J. W., Hannington, M. D., Tivey, M. K., Hansteen, T., Williamson, N. M. B., Stewart, M., et al. (2016). Precipitation and growth of barite within hydrothermal vent deposits from the Endeavour Segment, Juan de Fuca Ridge. *Geochimica et Cosmochimica Acta*, *173*, 64–85. https://doi.org/10.1016/j.gca.2015.10.021

Juniper, S. K., Tunnicliffe, V., & Fontaine, A. R. (1988). Biological influences on mineral deposition at deep-sea hydrothermal vents. *NOAA National Undersea Research Program Report*, *88*(4), 99–118.

Kajiwara, Y., & Krouse, H. R. (1971). Sulfur Isotope Partitioning in Metallic Sulfide Systems. *Canadian Journal of Earth Sciences*, *8*(1397).

Kase, K., Yamamoto, M., & Shibata, T. (1990). Copper-rich sulfide deposit 23°N, Mid-Atlantic Ridge: Chemical composition, mineral chemistry, and sulfur isotopes. In R. Detrick, J. Honnorez, W. B. Bryan, & T. Juteau (Eds.), *Proceedings of the Ocean Drilling Programm, Scientific Results* (Vol. 106/109, pp. 163–177). College Station.

Keith, M., Häckel, F., Haase, K. M., Schwarz-Schampera, U., & Klemd, R. (2016). Trace element systematics of pyrite from submarine hydrothermal vents. *Ore Geology Reviews*, *72*, 728–745. https://doi.org/10.1016/j.oregeorev.2015.07.012

Knott, R., Fouquet, Y., Honnorez, J., Petersen, S., & Bohn, M. (1998). Petrology of hydrothermal mineralization: a vertical section through the TAG mound. *Proceedings of the Ocean Drilling Program: Scientific Results*, *158*, 5–26. https://doi.org/10.2973/odp.proc.sr.158.201.1998

Krasnov, S. G., Cherkashev, G. A., Stepanova, T. V., Batuyev, B. N., Krotov, A. G., Malin, B. V., et al. (1995). Detailed geological studies of hydrothermal fields in the North Atlantic. In L. M. Parson, C. L. Walker, & D. R. Dixon (Eds.), *Hydrothermal Vents and Processes* (pp. 43–64). Geological Society Special Publication.

Langmuir, C., Humphris, S., Fornari, D., Van Dover, C., Von Damm, K., Tivey, M. K., et al. (1997). Hydrothermal vents near a mantle hot spot: the Lucky Strike vent field at 37°N on the Mid-Atlantic Ridge. *Earth and Planetary Science Letters*, *148*(1–2), 69–91. https://doi.org/10.1016/S0012-821X(97)00027-7

Langmuir, C. H., Klinkhammer, G., Bougault, H., & and Shipboard Scientific Party. (1992). *FAZAR Cruise Report*. Palisades, N.Y.

Layton-Matthews, D., Peter, J. M., Scott, S. D., & Leybourne, M. I. (2008). Distribution , Mineralogy , and Geochemistry of Selenium in Felsic Volcanic-Hosted Massive Sulfide Deposits of the Finlayson Lake District , Yukon Territory , Canada. *Economic Geology*, *103*, 61–88.

Lein, A. Y., Bogdanov, Y. A., Maslennikov, V. V., Li, S., Ulyanova, N. V., Maslennikova, S. P., & Ulyanov, A. A. (2010). Sulfide Minerals in the Menez Gwen Nonmetallic Hydrothermal Field (Mid Atlantic Ridge). *Lithology and Mineral Resources*, *45*(4), 305–323. https://doi.org/10.1134/S0024490210040012

Liao, S., Tao, C., Li, H., Barriga, F. J. A. S., Liang, J., Yang, W., et al. (2018). Bulk geochemistry, sulfur isotope characteristics of the Yuhuang-1 hydrothermal field on the ultraslow-spreading Southwest Indian Ridge. *Ore Geology Reviews*, *96*(April), 13–27. https://doi.org/10.1016/j.oregeorev.2018.04.007

Lisitsyn, A. P., Bogdanov, Y. A., & Gurvich, E. G. (1990). *Hydrothermal formations of the ocean rift zone*. Nauk Publisher.

Lisitsyn, A. P., Lapukhov, A. S., Simonov, V. A., Sidenko, N. V., Mazurov, M. P., Bogdanov, Y. A., & Batuev, V. N. (1999). Noble metals in ore-forming hydrothermal systems of modern oceans. *Doklady Earth Sciences*, *369*, 1198–1200.

Lydon, J. W. (1988). Ore deposit models 14. Volcanogenic massive sulphide deposits. Part 2: genetic models. *Geoscience Canada*, *15*(1), 43–65.

Marques, A. F., Barriga, F. J. A. S., & Scott, S. D. (2007). Sulfide mineralization in an ultramafic-rock hosted seafloor hydrothermal system : From serpentinization to the formation of Cu–Zn–(Co)-rich massive sulfides. *Marine Geology*, *245*, 20–39. https://doi.org/10.1016/j.margeo.2007.05.007

Martin, A. J., Keith, M., McDonald, I., Haase, K. M., McFall, K. A., Klemd, R., & MacLeod, C. J. (2019). Trace element systematics and ore-forming processes in mafic VMS deposits: Evidence from the Troodos ophiolite, Cyprus. *Ore Geology Reviews*, *106*(January), 205–225. https://doi.org/10.1016/j.oregeorev.2019.01.024

McDermott, J. M., Ono, S., Tivey, M. K., Seewald, J. S., Shanks, W. C., & Solow, A. R. (2015). Identification of sulfur sources and isotopic equilibria in submarine hot-springs using multiple sulfur isotopes. *Geochimica et Cosmochimica Acta*, *160*, 169–187. https://doi.org/10.1016/j.gca.2015.02.016

Melekestseva, I. Y., Maslennikov, V. V., Tret'yakov, G. A., Nimis, P., Beltenev, V. E.,

Rozhdestvenskaya, I. I., et al. (2017). Gold-And silver-rich massive sulfides from the semenov-2 hydrothermal field, 13°31.13'N, Mid-Atlantic ridge: A case of magmatic contribution? *Economic Geology*, *112*(4), 741–773. https://doi.org/10.2113/econgeo.112.4.741

Miranda, J. M., Luis, J. F., Lourenço, N., & Santos, F. M. (2005). Identification of the magnetization low of the Lucky strike hydrothermal vent using surface magnetic data. *Journal of Geophysical Research: Solid Earth*, *110*(4), 1–9. https://doi.org/10.1029/2004JB003085

Monecke, T., Petersen, S., Hannington, M. D., Grant, H., & Samson, I. M. (2016). The Minor Element Endowment of Modern Sea-Floor Massive Sulfi des and Comparison with Deposits Hosted in Ancient Volcanic Successions. In P. L. Verplanck & M. W. Hitzman (Eds.), *Rare earth and critical elements in ore deposits* (Vol. 18, pp. 245–306). Littleton, Colorado: Reviews in Economic Geology.

Morgan, C. L., & Selk, B. W. (1984). Ore assays of massive sulfides from three spreading centers. *Proceedings of the Annual Offshore Technology Conference*, *1984-May*, 9–16. https://doi.org/10.4043/4777-ms

Mozgova, N. N., Efimov, A. V., Borodaev, Y. S., Krasnov, S. G., Cherkashev, G. A., Stepanova, T. V., & Ashadze, A. M. (1999). Mineralogy and chemistry of massive sulfides from the Logatchev Hydrothermal Field (14°45' N Mid-Atlantic Ridge). *Exploration and Mining Geology*, *8*, 379–395.

Mozgova, N. N., Trubkin, N. V., Borodaev, Y. S., Cherkashev, G. A., Stepanova, T. V., Semkova, T. A., & Uspenskaya, T. Y. (2008). Mineralogy of massive sulfides from the Ashadze hydrothermal field 13°N, Mid-Atlantic Ridge. *Canadian Mineralogist*, *46*, 545–567.

Murowchick, J. B., & Barnes, H. L. (1986). Marcasite precipitation from hydrothermal solutions. *Geochimica et Cosmochimica Acta*, *50*(12), 2615–2629. https://doi.org/10.1016/0016-7037(86)90214-0

Murphy, P. J., & Meyer, G. (1998). A gold-copper association in ultramafic-hosted hydrothermal sulfides from the Mid-Atlantic ridge. *Economic Geology*, *93*, 1076–1083.

Ohmoto, H., & Lasaga, A. C. (1982). Kinetics of reactions between aqueous sulfates and sulfides in hydrothermal systems. *Geochimica et Cosmochimica Acta*, *46*(10), 1727–1745. https://doi.org/10.1016/0016-7037(82)90113-2

Ohmoto, H., & Rye, R. O. (1979). Isotope of sulfur and carbon. In H. L. Barnes (Ed.), *Geochemistry of Hydrothermal deposits* (pp. 509–567). New York: John Wiley and Sons.

Ondréas, H., Cannat, M., Fouquet, Y., Normand, A., Sarradin, P. M., & Sarrazin, J. (2009). Recent volcanic events and the distribution of hydrothermal venting at the Lucky Strike hydrothermal field, Mid-Atlantic Ridge. *Geochemistry, Geophysics, Geosystems*, *10*(2). https://doi.org/10.1029/2008GC002171

Ono, S., Shanks, W. C., Rouxel, O. J., & Rumble, D. (2007). S-33 constraints on the seawater sulfate contribution in modern seafloor hydrothermal vent sulfides. *Geochimica et Cosmochimica Acta*, *71*(5), 1170–1182. https://doi.org/10.1016/j.gca.2006.11.017

Palarea-Albaladejo, J., Martín-Fernández, J. A., & Buccianti, A. (2014). Compositional methods for estimating elemental concentrations below the limit of detection in practice using R. *Journal of Geochemical Exploration*, *141*, 71–77. https://doi.org/10.1016/j.gexplo.2013.09.003

Pawlowsky-Glahn, V., & Egozcue, J. J. (2006). Compositional data and their analysis : an introduction. *Geological Society, London, Special Publications*, *264*, 1–10.

Peresypkin, V. I., Lein, A. Y., Bogdanov, Y. A., & Nortinkov, N. S. (1999). On the nature of lipids in hydrothermal formations at the Broken Spur and vent fields of the Mid-Atlantic Ridge. *Exploration and Mining Geology*, *8*, 365–377.

Pester, N. J., Reeves, E. P., Rough, M. E., Ding, K., Seewald, J. S., & Seyfried, W. E. (2012). Subseafloor phase equilibria in high-temperature hydrothermal fluids of the Lucky Strike Seamount. *Geochimica et Cosmochimica Acta*, *90*, 303–322. https://doi.org/10.1016/j.gca.2012.05.018

Petersen, S., Herzig, P. M., & Hannington, M. D. (2000). Third dimension of a presently forming VMS deposit: TAG hydrothermal mound, Mid-Atlantic Ridge, 26°N. *Mineralium Deposita*, *35*(2–3), 233–259. https://doi.org/10.1007/s001260050018

Petersen, S., Krätschell, A., Augustin, N., Jamieson, J., Hein, J. R., & Hannington, M. D. (2016). News from the seabed – Geological characteristics and resource potential of deep-sea mineral resources. *Marine Policy*, *70*, 175–187. https://doi.org/10.1016/j.marpol.2016.03.012

Rona, P. A. (2003). Resources of the sea floor. *Science*, *299*(5607), 673–674. https://doi.org/10.1126/science.1080679

Rona, P. A., Hannington, M. D., Raman, C. V., Thompson, G., Tivey, M. K., Humphris, S. E., et al. (1993). Active and relict sea-floor hydrothermal mineralization at the TAG hydrothermal field, mid-Atlantic ridge. *Economic Geology*, *88*(8), 1989–2017. https://doi.org/10.2113/gsecongeo.88.8.1989

de Ronde, C. E. J., Massoth, G. J., Butterfield, D. A., Christenson, B. W., Ishibashi, J., Ditchburn, R. G., et al. (2011). Submarine hydrothermal activity and gold-rich mineralization at Brothers Volcano, Kermadec Arc, New Zealand. *Mineralium Deposita*, *46*(5), 541–584. https://doi.org/10.1007/s00126-011-0345-8

Rouxel, O., Fouquet, Y., & Ludden, J. N. (2004). Subsurface processes at the lucky strike hydrothermal field, Mid-Atlantic ridge: Evidence from sulfur, selenium, and iron isotopes. *Geochimica et Cosmochimica Acta*, *68*(10), 2295–2311. https://doi.org/10.1016/j.gca.2003.11.029

Samson, J. (1986). Compilation of Information on Polymetallic Sulfide Deposits and

Occurrences off the West Coast of Canada. *Canada Oil and Gas Lands Administration*, 1–58.

Sánchez-Mora, D, Jamieson, J. W., Cannat, M., Escartín, J., & Barreyre, T. (2022). Bulk geochemistry and in situ sulfur isotopes of hydrothermal deposits from the Lucky Strike vent field, Mid-Atlantic Ridge. *Zenodo*. https://doi.org/https://doi.org/10.5281/zenodo.6035032

Sánchez-Mora, D., Jamieson, J. W., Escartín, J., Barreyre, T., & Cannat, M. (submitted). Age and rates of formation of metal-rich hydrothermal deposits on the seafloor: example from the Lucky Strike Vent Field, Mid-Atlantic Ridge.

Sarradin, P. M., & Cannat, M. (2014). MOMARSAT2014 cruise, RV Pourquoi pas ? https://doi.org/10.17600/14000300

Sarradin, P. M., & Cannat, M. (2015). MOMARSAT2015 cruise, RV Pourquoi pas ? https://doi.org/10.17600/15000200

Seher, T., Crawford, W. C., Singh, S. C., & Cannat, M. (2010). Seismic layer 2A variations in the Lucky Strike segment at the Mid-Atlantic Ridge from reflection measurements. *Journal of Geophysical Research: Solid Earth*, *115*(7), 1–20. https://doi.org/10.1029/2009JB006783

Shanks, W. C. I. (2001). Stable Isotopes in Seafloor Hydrothermal Systems: Vent fluid, hydrothermal deposits, hydrothermal alteration, and microbial processes. In J. W. Valley & D. R. Cole (Eds.), *Stable Isotope Geochemistry* (pp. 469–525). Washington, D.C.: Reviews in Mineralogy & Geochemistry.

Singh, S. C., Crawford, W. C., Carton, H., Seher, T., Combier, V., Cannat, M., et al. (2006). Discovery of a magma chamber and faults beneath a Mid-Atlantic Ridge hydrothermal field. *Nature*, *442*(7106), 1029–1032. https://doi.org/10.1038/nature05105

Thompson, G., Humphris, S. E., Schroeder, B., Sulanowska, M., & Rona, P. A. (1988). Active vents and massive sulfides at 26°N (TAG) and 23°N (Snakepit) on the Mid-Atlantic Ridge. *Canadian Mineralogist*, *26*, 697–711.

Tivey, M. K., & Delaney, J. R. (1986). Growth of large sulfide structures on the Endeavour segment of the Juan de Fuca ridge. *Earth and Planetary Science Letters*, *77*(3–4), 303–317. https://doi.org/10.1016/0012-821X(86)90142-1

Tivey, M. K. (2007). Generation of Seafloor Hydrothermal Vent Fluids and Associated Mineral Deposits. *Oceanography*, *20*(1), 50–65. https://doi.org/10.5670/oceanog.2007.80

Tivey, M. K., Stakes, D. S., Cook, T. L., Hannington, M. D., & Petersen, S. (1999). A model for growth of steep-sided vent structures on the Endeavour Segment of the Juan de Fuca Ridge: Results of a petrologic and geochemical study. *Journal of Geophysical Research: Solid Earth*, *104*(B10), 22859–22883. https://doi.org/10.1029/1999JB900107

Toffolo, L., Nimis, P., Tret'yakov, G. A., Melekestseva, I. Y., & Beltenev, V. E. (2020). Seafloor massive sulfides from mid-ocean ridges: Exploring the causes of their geochemical variability with multivariate analysis. *Earth-Science Reviews*, *201*(February 2019), 102958.

https://doi.org/10.1016/j.earscirev.2019.102958

Wang, Y., Han, X., Petersen, S., Jin, X., Qiu, Z., & Zhu, J. (2014). Mineralogy and geochemistry of hydrothermal precipitates from Kairei hydrothermal field, Central Indian Ridge. *Marine Geology*, *354*, 69–80. https://doi.org/10.1016/j.margeo.2014.05.003

Wang, Y., Han, X., Zhou, Y., Qiu, Z., Yu, X., Petersen, S., et al. (2021). The Daxi Vent Field: An active mafic-hosted hydrothermal system at a non-transform offset on the slow-spreading Carlsberg Ridge, 6°48′N. *Ore Geology Reviews*, *129*(April 2020), 103888. https://doi.org/10.1016/j.oregeorev.2020.103888

Webber, A. P., Roberts, S., Murton, B. J., & Hodgkinson, M. R. S. (2015). Geology, sulfide geochemistry and supercritical venting at the Beebe Hydrothermal Vent Field, Cayman Trough. *Geochemistry, Geophysics, Geosystems*, (February 2013), 2661–2678. https://doi.org/10.1002/2015GC005879.Received

Zeng, Z., Ma, Y., Chen, S., Selby, D., Wang, X., & Yin, X. (2017). Sulfur and lead isotopic compositions of massive sulfides from deep-sea hydrothermal systems: Implications for ore genesis and fluid circulation. *Ore Geology Reviews*, *87*, 155–171. https://doi.org/10.1016/j.oregeorev.2016.10.014

	Mineral	Texture	Mineral assemblage	$\delta^{34}S$ (‰)	SEM
Capelinhos site					
MOM14-PL583-ROC4_Cpy1	Cpy	euhedral/massive	marcasite-chalcopyrite	7.7	0.5
MOM14-PL583-ROC4_Cpy3	Cpy	massive	chalcopyrite	6.3	0.2
MOM14-PL583-ROC4_Cpy1	Cpy	massive	chalcopyrite	6.5	0.2
MOM14-PL583-ROC4_Cpy2	Cpy	massive	chalcopyrite	6.5	0.2
MOM14-583-ROC1-S _Cpy1	Cpy	euhedral	marcasite-chalcopyrite	7.2	0.3
MOM14-583-ROC1-S _Cpy2	Cpy	euhedral/massive	marcasite-chalcopyrite	4.7	0.6
MOM13-528-ROC1-S_Cp1	Cpy	cpy disease	sphalerite-chalcopyrite	8.7	0.5
MOM13-528-ROC1-S_Mrc2	Mrc	plumose	marcasite-barite-sphalerite	3.4	0.3
MOM13-528-ROC1-S_Mrc1	Mrc	plumose	marcasite-barite-sphalerite	3.9	0.4
MOM14-583-ROC1-S_Mrc2	Mrc	massive/subhedral	marcasite-chalcopyrite	5.2	0.3
MOM14-583-ROC1-S_Mrc1	Mrc	atoll/ring	marcasite-chalcopyrite	4.0	0.8
MOM14-PL583-ROC4_Mrc1	Mrc	atoll/ring	marcasite	1.7	0.6
MOM14-PL583-ROC4_Mrc2	Mrc	euhedral/massive	marcasite	4.4	0.7
MLSHF-Chimiste					
MOM15-PL607_ROC3_Mrc1	Mrc	euhedral	marcasite	-0.5	0.3
MLSHF-Isabel					
MOM15-PL607_11_ROC5_Cpy1	Cpy	massive	marcasite-chalcopyrite	2.8	0.2
MOM15-PL607_11_ROC5_Cpy2	Cpy	euhedral	marcasite-chalcopyrite	2.8	0.5
MOM15-PL607_11_ROC5_Mrc1	Mrc	colloform	marcasite-chalcopyrite	-2.4	0.3
MOM15-PL607_11_ROC5_Mrc2	Mrc	plumose	marcasite-chalcopyrite	-0.7	0.4
MLSHF-Sintra					
MOM11-452-ROC3_Cpy2	Cpy	euhedral/massive	chalcopyrite-sphalerite	2.0	0.3
MOM11-452-ROC3_Cpy1	Cpy	euhedral/massive	chalcopyrite-sphalerite	3.3	0.4
MOM11-452-ROC3_Cpy3	Cpy	euhedral/massive	chalcopyrite	2.1	0.3
MOM11-452-ROC2_Cpy2	Cpy	massive	chalcopyrite-marcasite-covellite	4.7	0.4
MOM11-452-ROC2_Cpy1	Cpy	massive	chalcopyrite-marcasite-covellite	6.0	0.4
MOM11-452-ROC3_Mrc1	Mrc	atoll/ring	marcasite-chalcopyrite	-0.7	0.3
MOM11-452-ROC1_Mrc2	Mrc	colloform	marcasite-barite	-0.6	0.4
MOM12-502-ROC1_Mrc1	Mrc	colloform	marcasite-barite	1.1	0.5
MOM11-452-ROC1_Mrc1	Mrc	colloform	marcasite-barite	1.1	0.6
MOM11-452-ROC2_Mrc1	Mrc	euhedral	marcasite-chalcopyrite	0.9	0.3
MLSHF-Tour Eiffel					
MOM13-532-ROC2_Cpy1	Cpy	massive	marcasite-chalcopyrite	4.3	0.3
MOM11-457-ROC8_Cpy1	Cpy	massive	chalcopyrite-sphalerite	4.8	0.3
MOM14-579-ROC1_Cpy3	Cpy	euhedral	chalcopyrite-sphalerite	5.3	0.4
MOM13-532-ROC2_Mrc1	Py	euhedral/massive	marcasite-chalcopyrite	1.6	0.3
MOM12-504-ROC1_Mrc1	Mrc	colloform	barite-marcasite	-0.3	0.6
MOM11-457-ROC8_Mrc1	Mrc	plumose	marcasite-barite	0.1	0.4
MOM13-532-ROC1_Mrc2	Mrc	colloform	marcasite	0.9	0.3
MOM13-532-ROC1_Mrc6	Mrc	colloform	marcasite	0.9	0.3
MOM13-532-ROC1_Mrc4	Mrc	colloform	marcasite	1.0	0.2
MOM13-532-ROC1_Mrc3	Mrc	colloform	marcasite	1.1	0.2
MOM13-532-ROC1_Mrc5	Mrc	colloform	marcasite	1.3	0.3
MOM13-532-ROC1_Mrc7	Mrc	massive	marcasite-sphalerite	1.4	0.5
MOM13-532-ROC1_Mrc1	Mrc	colloform	marcasite	1.5	0.7
MOM14-579-ROC1_Mrc2	Mrc	plumose	barite-marcasite	1.3	0.3
MOM14-579-ROC1_Mrc1	Mrc	atoll/ring	barite-marcasite	2.0	0.3
MLSHF-White Castle					

MOM15-603-ROC6_Cpy1	Cpy	euhedral	chalcopyrite-sphalerite	3.1	0.4
MOM15-603-ROC6_Mrc1	Py	euhedral	marcasite	1.5	0.3
MLSHF-Y3					
LS-BS-WHOI_Cpy3	Cpy	euhedral	chalcopyrite-sphalerite	1.0	0.3
LS-BS-WHOI_Cpy1	Cpy	euhedral	chalcopyrite-sphalerite	1.8	0.4
LS-BS-WHOI_Cpy2	Cpy	euhedral	chalcopyrite-sphalerite	1.8	0.5
MOM11-454-ROC7_Cpy1	Cpy	euhedral	chalcopyrite-sphalerite	3.7	0.4
LS-BS-WHOI_Mrc1	Mrc	plumose	marcasite-barite	-1.0	0.3
MOM11-454-ROC7_Mrc1	Mrc	plumose	marcasite	-2.5	0.2
MOM11-454-ROC7_Mrc2	Py	plumose/euhedral	marcasite	-0.8	0.3

Analyte Symbol	Latitude	Longitude	Description	IGSN	Cu (wt.%)	Zn (wt.%)	Pb (ppm)	Fe (wt.%)	S (wt.%)	Si (wt.%)	Al (wt.%)	Ca (wt.%)	Na (wt.%)	Mg (wt.%)	Ba (ppm)	Sr (ppm)	Mo (ppm)	V (ppm)	Ni (ppm)	Co (ppm)	Se (ppm)	Au (ppb)	Ag (ppm)	As (ppm)	Ga (ppm)	Ge (ppm)	Sb (ppm)	Cd (ppm)	Tl (ppm)	In (ppm)	Sn (ppm)	Mn (ppm)
Detection Limit					0.0002	0.001	0.8	0.01	0.01	0.01	0.01	0.01	0.001	0.01	20	3	1	5	10	0.1	0.5	2	2	1	0.2	0.7	0.1	2	0.1	0.2	0.5	3
Analysis Method					FUS	INAA	FUS	INAA	FUS	FUS	FUS	FUS	INAA	FUS	INAA	FUS	FUS	FUS	FUS	INAA	INAA	INAA	INAA	INAA	FUS	FUS	INAA	FUS	FUS	FUS	FUS	FUS
Capelinhos (1678 mbsl)																																
MOM14-583-ROC1-S	37.28973	-32.281042	Block from the base of Capelinhos edifice	CNRS0000007069	5.4	1.01	113	21.8	27	11.9	0.04	0.09	0.12	<0.01	45200	1150	33	<5	<10	277	<0.5	258	22	128	27.5	6.8	11.4	43	5.4	10.1	3.7	55
MOM14-PL583-ROC4	37.289418	-32.263983	Fragment A of active chimney	CNRS0000007072	5.09	2.49	193	42.4	50.1	0.04	0.03	0.48	0.08	<0.01	1760	97	37	<5	10	158	131	256	21	291	27.4	14.8	15	55	16.2	2.6	5.3	76
MOM14-PL583-ROC4	37.289418	-32.263983	Fragment B of active chimney	CNRS0000007072	11.4	1.53	137	40	45.3	0.22	0.11	0.05	0.22	<0.01	330	20	40	9	10	258	150	237	22	229	15	10.8	11.4	30	5.5	6	3.3	38
MOM13-528-ROC1-S	37.289467	-32.263972	Block from the base of Capelinhos edifice	N/A	0.0459	6.64	716	35.4	46.9	0.17	0.05	0.07	0.16	0.01	12900	737	69	<5	10	14.1	<0.5	323	39	236	51.4	22.8	49.9	213	61.9	1	1	91
Y3 (1730 mbsl)																																
MOM11-454-ROC7	37.291867	-32.277817	Base of small active chimney	CNRS0000007017	4.02	7.57	489	31.5	41.5	1.56	0.5	0.19	0.3	0.02	19300	850	318	110	10	337	127	625	88	307	45.8	33.2	23.7	288	44	1.4	2.5	634
White Castle (1705 mbsl)																																
MOM15-603-ROC5	37.28973	-32.281042	Block from active edifice	CNRS0000007099	1.41	27.6	887	12.3	34.7	2.94	0.64	0.07	0.25	0.03	4960	239	121	<5	<10	64.6	42.6	748	152	277	63.8	60.8	50	1250	27.6	0.7	3.5	464
MOM15-603-ROC6	37.28973	-32.281042	Block from active edifice	CNRS0000007100	10.1	0.614	209	27.3	35.8	5.45	0.36	0.1	0.18	0.04	38300	1700	351	51	30	604	237	205	9	142	8.2	21.9	5	17	10.7	3.4	2.3	193
ial graben to the W (1612 mbsl)																																
MOM15-605-ROC2	37.295229	-32.284963	From inactive site	CNRS0000007103	0.035	0.048	31.3	0.56	6.29	0.6	<0.01	0.16	0.12	0.02	444000	5940	7	6	10	7.4	<0.5	8	<2	14	1.1	3.4	0.8	<2	<0.1	<0.2	1.7	369
Tour Eiffel (1696 mbsl)																																
MOM11-457-ROC8	37.289033	-32.275667	Small inactive chimney W of Tour Eiffel	CNRS0000007018	1.52	37.4	823	17.5	38.5	0.95	0.08	0.1	0.06	<0.01	34500	1040	59	6	10	33	<0.5	2030	278	346	354	68.2	166	1700	42.6	5.7	1.1	424
MOM14-579-ROC1	37.290722	-32.281038	Small inactive chimney	CNRS0000007062	7.36	7.62	454	28.5	36.7	5.36	0.61	0.1	0.19	0.01	23800	667	167	122	40	107	179	724	76	387	62.6	29.8	36.9	288	38.5	4.2	2.3	349
MOM13-532-ROC1	37.288933	-32.275417	Block in the E slope of Tour Eiffel		0.012	0.128	746	26.3	33.2	4.63	<0.01	0.1	0.14	<0.01	99400	2080	25	<5	20	48.5	<0.5	309	<2	449	1.7	23.1	2.3	4	151	<0.2	1	205
MOM13-532-ROC2	37.288933	-32.275417	Block of sulfide at base of Tour Eiffel	N/A	19.4	0.037	19.9	31.7	41.3	0.51	0.18	0.07	0.28	0.05	950	48	22	12	10	167	2570	73	<2	99	1.7	5.7	1.6	<2	1.2	2.5	6.3	60
n SW of Tour Eiffel (1691 mbsl)																																
MOM12-504-ROC1	37.288583	-32.276333	Block in inactive area 85 m SW of Tour Eiffel	CNRS0000007053	1.02	10.8	502	11.2	17.7	13.6	0.28	0.15	0.38	0.03	112000	1420	66	35	20	50.6	<0.5	1750	165	642	55.3	43	82.8	291	21.6	0.6	0.6	1240
Sintra (1630 mbsl)																																
MOM11-452-ROC1	37.292083	-32.274717	Small inactive chimney on sulfide-rich basement at the base of Sintra	CNRS0000007011	2.45	0.554	993	38.8	38.1	0.91	0.15	0.84	0.41	0.11	14200	407	67	131	20	467	69.9	1340	49	635	46.5	19.9	39	9	23.4	12.7	1.1	1830
MOM11-452-ROC2	37.292083	-32.2747	Fragments of inactive chimney	CNRS0000007012	25.6	0.593	379	31.9	37.4	0.32	0.15	0.04	0.21	0.02	310	24	100	20	10	225	346	1010	94	223	36.5	19.5	19	25	6.5	10.5	4.2	113
MOM11-452-ROC3	37.292033	-32.274717	Fragments of inactive chimney	CNRS0000007013	26.4	1.57	306	26.7	33.5	1.77	0.26	0.06	0.21	0.03	2870	41	59	16	10	47.5	106	677	59	242	28	24.1	28	59	13.4	6.9	1.6	153
MOM12-502-ROC1	37.292167	-32.2750	Active chimney	CNRS0000007051	0.036	5.08	541	4.74	9.41	0.3	<0.01	0.17	0.29	<0.01	381000	5110	11	<5	<10	8.5	<0.5	369	89	168	10.4	50.9	29.5	98	36.9	<0.2	0.9	65
Isabel (1703 mbsl)																																
MOM15-PL607_ROC5	37.28912	-32.277405	Sulfide block	CNRS0000007108	13.5	0.22	177	35.1	40.3	0.51	0.23	0.05	0.23	0.03	380	23	267	44	10	409	907	539	44	268	5.1	6.9	6.3	6	9.8	6.3	5.9	211
Chimiste (1687 mbsl)																																
MOM15-PL607_ROC3	37.289291	-32.276545	Sulfide block	CNRS0000007106	1.27	0.562	354	30.3	38.6	12.3	0.19	0.04	0.2	<0.01	270	20	69	<5	20	89.2	28.9	496	59	477	3.4	8.1	9.6	27	18.4	0.3	1	353
Temperature probe precipitates																																
Cyprès (1740 mbsl)																																
MOM14-HN29008-ROCK	37.290787	-32.280972	Precipitate on temperature probe	N/A	8.5	0.049	8.1	44.3	48.5	0.08	0.03	0.34	0.05	0.02	<20	36	6	<5	60	559	227	37	6	85	0.7	5.1	0.5	<2	<0.1	8.4	17.7	11
Crystal (1730 mbsl)																																
HT010-CR12	37.29088	-32.28202	Precipitate on temperature probe	N/A	2.41	2.12	230	10.3	29.2	0.42	0.17	17.4	0.21	0.07	7420	2100	444	57	1450	101	70.6	189	28	97	12.2	9.7	12.4	122	9.2	2.5	3	92
Cimendef (1702 mbsl)																																
Y3 (1730 mbsl)																																
MOM14-HT007-ROCK	37.288083	-32.275838	Precipitate on temperature probe	N/A	5.25	0.098	18.2	44.8	50.8	0.22	0.09	1	0.07	0.04	560	132	11	<5	20	86.8	385	47	<2	96	1.4	5.8	1.1	3	1.3	1.7	2.2	25
LS-BS-WHOI	37.29187	-32.27785	Precipitate on temperature probe	N/A	15.2	2.13	201	30.1	35.6	3.27	0.24	0.13	0.1	<0.01	32300	1360	212	58	30	198	490	228	52	120	17.8	19.9	8.3	92	21	3.1	2.3	341